THE ASTROPHYSICAL JOURNAL, 460:993–1018, 1996 April 1

A THEORY OF EXTRASOLAR GIANT PLANETS

D. SAUMON,[1,2] W. B. HUBBARD,[2] A. BURROWS,[3] T. GUILLOT,[2] J. I. LUNINE,[2] AND G. CHABRIER[4]
Received 1995 August 10; accepted 1995 October 18

ABSTRACT

We present a broad suite of models of extrasolar giant planets (EGPs), ranging in mass from 0.3 to 15 Jupiter masses. The models predict luminosity (both reflected and emitted) as a function of age, mass, deuterium abundance, and distance from parent stars of various spectral types. We also explore the effects of helium mass fraction, rotation rate, and the presence of a rock-ice core. The models incorporate the most accurate available equation of state for the interior, including a new theory for the enhancement of deuterium fusion by electron screening, which is potentially important in these low-mass objects, The results of our calculations reveal enormous sensitivity of EGPs to the presence of the parent star, particularly for G and earlier spectral types. They also show a strong sensitivity of the flux contrast in the mid-infrared, between parent star and EGP, to the mass and age of the EGPs. We interpret our results in terms of search strategies for ground- and space-based observatories in place or anticipated in the near future.

Subject headings: planetary systems

1. INTRODUCTION

The questions of the existence and properties of other planetary systems represent one of the philosophical centerpieces of modern astrophysics. Planetary systems are an end state of the process of star formation, and the existence of planets imposes an important set of physical constraints on that process. Characteristics of planets provide information about the angular momentum content and evolution of the system, the lifetime of the disks, and the nature of the energetic processes associated with the pre–main-sequence star itself.

Giant planets are of particular interest, both because they are most detectable with current and envisioned technologies and because they pose a puzzle for planet formation. Our prototypes of giant planets are Jupiter and Saturn, which are composed primarily of hydrogen and helium in roughly solar proportions but which differ in detail from solar composition in that they are enhanced in metals by about 1 order of magnitude, with a substantial quantity of these heavier elements concentrated toward their centers.

The purpose of this paper is to provide accurate and extensive models of extrasolar giant planet brightnesses and dimensions as a function of age, composition, and mass, both as a guide to what stars (spectral type, age) around which to search for giant planets and as a tool for interpreting the results of any positive detections. It has long been recognized that essentially the same physics governs the structure and evolution of the suite of electron-degenerate and hydrogen-rich objects, ranging from brown dwarfs (at the high-mass end) to Jupiters and Saturns (at the low-mass end). Except for an initial study by our group (Burrows et al. 1995), no one has quantitatively mapped out the properties of objects between the mass of giant planets in our solar system and the traditional brown dwarfs (greater than 10–20 M_J, where M_J is the mass of Jupiter), which we term extrasolar giant planets (EGPs).

Earlier work generally consists of evolutionary models of planets of 1 M_J and below, beginning with Graboske et al. (1975, hereafter GPGO; but see Hubbard 1977). This work calculates the evolution of the low-mass objects Jupiter and Saturn from an age of 10^7 years to the present (4.5 Gyr). Working down from higher masses, Grossman & Graboske (1973; GG73) extended their calculations of brown dwarf evolution to as low as 12 M_J, but had to limit their study to ages less than about 0.1 Gyr. Black (1980) used the results of GG73 and GPGO to infer simple power-law relations for the variation of luminosity L and radius R as a function of mass M and time t. Black's relations are roughly valid for objects close in mass to 1 M_J and close in age to 4.5 Gyr. However, as we discuss below, Black's formulae become very inaccurate at earlier ages and at larger masses.

The scope of this paper is as follows. Our lower mass limit is the mass of Saturn (0.3 M_J), and our upper mass limit is 15 M_J, which takes us to objects that would generally be considered brown dwarfs. Our baseline models for EGPs are composed of hydrogen and helium, with a helium mass fraction $Y = 0.25$ and with a metals mass fraction $Z \approx 0.02$, with the latter playing no significant role in the interior structure. However, we also examine the effect of enhancing metals well above solar composition. Our theory does not include objects similar to the ice giant planets Uranus and Neptune. These belong to a different class of object because they contain minor hydrogen-helium fractions, and their masses and luminosities are an order of magnitude smaller than those of Jupiter and Saturn.

Our theory starts with the assumption that EGPs have been somehow formed from an initially gaseous, high-entropy state. Current theoretical models for forming giant planets require relatively rapid accretion of large amounts of protoplanetary disk gas onto a core of rocky and icy material (Podolak, Hubbard, & Pollack 1993). Models of our own protoplanetary disk, or solar nebula, suggest that the timescale for accumulating a giant planet's solid core is long enough that the gaseous accretion stage may potentially be truncated, as appears to have happened for Uranus

[1] Hubble Postdoctoral Fellow.
[2] Department of Planetary Sciences, University of Arizona, Tucson, AZ 85721; dsaumon, guillot, hubbard, jlunine@lpl.arizona.edu.
[3] Departments of Physics and Astronomy, University of Arizona, Tucson, AZ 85721; burrows@cobalt.physics.arizona.edu.
[4] Centre de Recherche Astrophysique de Lyon (UMR 142 CNRS), Ecole Normale Supérieure, 46, Allée d'Italie, 69364 Lyon Cedex 07, France; chabrier@physique.ens-lyon.fr.

and Neptune. Although this problem appears to have been solved for Jupiter and Saturn (Lissauer 1995), a potential complication is that the tidal effects of such a growing object may cause a gap in the gas disk to form, which truncates or greatly slows accretion (Lin & Papaloizou 1993). Very recent observations (Zuckerman, Forveille, & Kastner 1995) suggest that in many protoplanetary systems the bulk of the gas may be dissipated within a few million years, thus resurrecting the timescale problem, since timescale had previously been assumed to be at least several times longer. Further, recent models of protoplanetary disks seem to suggest that Jovian planet formation does not occur within roughly 5 AU, being relatively insensitive to the spectral type of the central star for $M \leq 1\ M_\odot$ (Boss 1995). If this is the case, the timescale problem would be common to giant planets forming around protostars of a wide range of masses.

Because of the seeming delicacy in arranging for the successful formation of a giant planet, Wetherill (1993) argued that Jupiters and Saturns may be rarities in planetary systems. If so, this would have interesting consequences for the habitability of terrestrial planets in other systems, since the giant planets have been very effective in sweeping cometary debris from our own solar system. Observations of the β Pictoris system suggest orders of magnitude more dust than in our own solar system, even relatively close to the central star (Backman, Gillett, & Witteborn 1992), and it is tempting to speculate that this system contains no giant planets to sweep the inner regions clear of small debris.

Walker et al. (1995) have monitored the radical velocity of 21 nearby stars, and find no Jupiter-mass planets on circular orbits of less than 15 yr periods. Since this survey is not definitive, it is fair to say that there is controversy in both the theory and the data about the mode of formation of giant planets, and consequently about how common they may be. We believe that this question must be settled observationally, and thus our motive is to provide extensive and quantitative predictions useful for observers who are trying to detect EGPs. The technologies now seem to be sensitive enough for direct detection by imaging from the ground and space (Angel 1994; Burrows et al. 1995), as well as by indirect techniques such as radial velocity (McMillan et al. 1994), precision astrometry (Gatewood 1987), microlensing (Gould & Loeb 1992), and photometric detection of transits of a giant planet (Borucki & Genet 1992).

In the present work, we use updated high-pressure thermodynamics, derived from two decades of laboratory and theoretical work (see, e.g., Van Horn & Ichimaru 1993; Chabier & Schatzman 1994), and an improved surface boundary condition to construct models ranging from Saturn and Jupiter up through 15 M_J. In § 2 we describe the physics used to model the atmospheres and interiors of these objects. Section 3 presents results of the model, comparing with the data on Jupiter and Saturn, and explores the nature of the deuterium-burning phase, the effects of varying the flux from the central star, the helium abundance, and the mass of heavy-element core. In § 4 we utilize our ensemble of new models to predict what extrasolar giant planets should look like, and how and where to target the searches.

2. INPUT PHYSICS TO THE MODELS

We follow the evolution of giant gaseous planets, with masses from 0.3 to 15 M_J, for 5 Gyr. The models are nonrotating and in hydrostatic equilibrium. We neglect the presence of metals in the interior of the planet, but the atmospheric surface boundary condition assumes a solar abundance of heavy elements. The effect of heavy elements concentrated in a central rock-ice core is discussed in § 3.3. The calculation is similar to the brown dwarf sequences of Burrows et al. (1993) and to the EGP results of Burrows et al. (1995), where additional information can be found. We upgrade the input physics of Burrows et al. (1993) by using a more accurate equation of state for H/He mixtures, extending the surface boundary condition to lower effective temperatures, and applying state-of-the-art screening corrections to the rate of the $^2D(p, \gamma)^3He$ nuclear reaction.

2.1. *The Surface Boundary Condition: Treatment of the Atmosphere*

Calculation of the evolution of fully adiabatic models of EGPs requires a surface condition which can be expressed in the form

$$T_{10} = f(g, T_{\rm eff}) , \quad (1)$$

where T_{10} is the temperature corresponding to the internal adiabat at a chosen pressure of 10 bars, and f is a function of the surface gravity g and the effective temperature $T_{\rm eff}$, which is determined from a grid of model atmospheres. Here $T_{\rm eff}$ is the effective temperature of a blackbody with the EGPs radius, whose thermal luminosity corresponds to the sum of the intrinsic luminosity of the EGP and the absorbed stellar luminosity. The absorbed luminosity is calculated using a Bond albedo of $A = 0.35$, which is characteristic of the giant planets of the solar system.

We have previously determined f for $T_{\rm eff} \geq 600$ K, for the X-model sequence of Burrows et al. (1993). For giant planets at lower values of $T_{\rm eff}$ and g, GPGO determined f in tabular form by integrating model atmospheres in the range

$$20\ {\rm K} \leq T_{\rm eff} \leq 1900\ {\rm K} , \quad (2)$$

and for two values of g, 40.39 and 2585 cm s^{-2}. GPGO took into account collision-induced absorption (CIA) opacity for H_2-H_2 and H_2-He, calculated by Linsky (1969), water opacity from Ferriso et al. (1966) up to 11000 cm^{-1}, ammonia opacity (at very low frequencies), and methane opacity (at very low frequencies).

Hubbard (1977) fitted an analytic form for f to the tabulated data of GPGO, with the result

$$T_{10} = 3.36 g^{-1/6} T_{\rm eff}^{1.243} \quad (3)$$

(all quantities in cgs units). However, this form is accurate only for $T_{\rm eff} \leq 200$ K. For $T_{\rm eff} > 200$ K, we find that a better fit is given by

$$T_{10} = 15.86 g^{-1/6} T_{\rm eff}^{0.95} . \quad (4)$$

Since the GPGO calculations do not extend to gravities greater than the present surface gravity of Jupiter (2600 cm s^{-2}), some extrapolation of relations (3) and (4) is required for the calculation of the evolution of objects more massive than Jupiter.

As long as CIA is the dominant source of thermal opacity, f is expected to have a weak dependence on g. To isolate the g-dependence, we can write the equation of hydrostatic equilibrium for the radiative portion of the planetary atmosphere as follows:

$$\frac{dP}{d\tau} = \frac{g}{\kappa} , \quad (5)$$

where τ is the optical depth and κ is the opacity per unit mass. For CIA, in which the opacity is proportional to the number density of molecules, we can write

$$\kappa = \alpha(T_{\rm eff})\,\frac{P}{T}\,, \tag{6}$$

where α is some function of $T_{\rm eff}$ which does not depend on P or T. In the radiative upper atmosphere we write the usual approximation for the $T(\tau)$ relation

$$T = 2^{-1/4}T_{\rm eff}(1 + \tfrac{3}{2}\tau)^{1/4}\,. \tag{7}$$

We assume that the atmosphere becomes convective and thus adiabatic for $\tau \sim 1$. Substituting equations (6) and (7) in equation (5) and integrating from $\tau = 0$ to $\tau = 1$ yields

$$P^2_{\tau=1} \propto g T_{\rm eff}/\alpha(T_{\rm eff})\,. \tag{8}$$

Hubbard (1977) assumed that in the adiabatic portion of the atmosphere, which commences at $\tau > 1$, $P \propto T^3$, or $P^2_{\tau=1} = P^2(T^6_{\tau=1}/T^6)$. Thus, at a fixed pressure of 10 bars, equation (8) leads to $T_{10} \propto g^{-1/6}$, in agreement with equations (3) and (4).

For hydrogen-helium adiabats in the temperature range considered (100 K $\leq T \leq$ 1000 K), the adiabatic relation is more accurately written as $P \propto T^{3.3}$, which leads to a slightly weaker dependence of T_{10} on g, viz., $T_{10} \propto g^{-1/6.6}$; we ignore this complication considering the crudity of the other approximations.

We adopt equations (3) and (4) for $T_{\rm eff} \leq 300$ K, and we use the X grid of surface conditions (Burrows et al. 1993) for $T_{\rm eff} \geq 600$ K. Simple interpolation is used to determine boundary conditions for objects which lie between the two ranges. Figure 1 shows, for six different values of g, the X surface conditions, and the surface conditions (eqs. [3]–[4]), along with the interpolation region. As the figure indicates, the actual g-dependence of T_{10} may be somewhat steeper than $g^{-1/6}$ for $T_{\rm eff} \leq 600$ K and for surface gravities greater

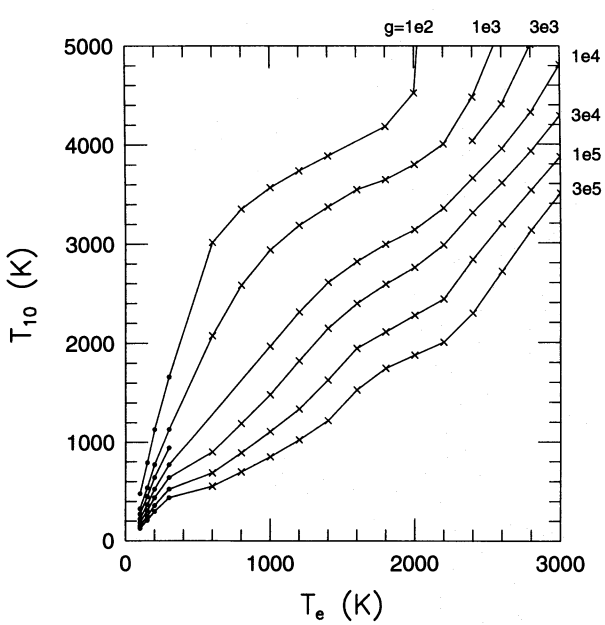

FIG. 1.—T_{10} vs. $T_{\rm eff}$ for various surface gravities (in cgs units). For $T_{\rm eff} \leq 300$ K, surface conditions (3–4) are used (*filled circles*). The upper two curves are constrained by the gravity range of the atmosphere models calculated by GPGO, while the lower three curves represent extrapolation, via eqs. (3)–(4), to higher gravities. For $T_{\rm eff} \geq 600$ K, the curves show the atmosphere models of the X sequence of Burrows et al. (1993).

than 10^4 cm s^{-2}. For improved results it will eventually be necessary to calculate atmosphere models in this range.

2.2. *Thermodynamics of the Interior*

Simple physical arguments and detailed calculations indicate that stars with masses below $\sim 0.3\ M_\odot$ (or $\sim 300\ M_J$) have fully convective interiors and that this state persists through the regime of brown dwarfs down to giant planets like Saturn. It follows from the high convective efficiency found in these low-$T_{\rm eff}$ objects that the interior structure is adiabatic. Models are obtained by integrating the equation of hydrostatic equilibrium along adiabats generated with the equation of state (EOS) of Saumon, Chabrier, & Van Horn (1995, hereafter SCVH), which was developed for applications to very low mass stars, brown dwarfs, and giant planets. In these relatively dense and cool objects, nonideal effects dominate the physics of the EOS, particularly at densities above ≈ 0.1 g cm^{-3}, where neutral particles (e.g., H_2) strongly repel each other and ultimately become pressure-ionized to form a strongly coupled plasma. These effects are carefully accounted for in the SCVH EOS, which is the most accurate available for these objects.

The SCVH EOS reproduces all relevant experimental results very well, except for the new measurements by Holmes, Ross, & Nellis (1995) on shock-compressed deuterium, which disagree with the SCVH EOS in the regime of pressure dissociation of H_2 molecules. The new data suggest a larger degree of dissociation than predicted by SCVH. This effect has potentially significant consequences for the interior of giant planets (Nellis, Ross, & Holmes 1995), but it is not included in the present work. Modifications of the EOS to bring it into agreement with the new measurements are currently under way.

Finally, we adopt a helium mass fraction of $Y = 0.25$ for the interior models. The sensitivity of the models to the helium mass fraction is discussed in § 3.3. We find that the calculated emissions of EGPs (§ 4.2) are barely affected when using a value of $Y = 0.28$.

2.3. *Screening Correction to the* ^{2}D$(p, \gamma)^3$He *Reaction Rate*

Marginal ignition of deuterium via the reaction ^{2}D$(p, \gamma)^3$He occurs in objects in the EGP mass range. The first study of this topic was by GG73, who found a deuterium main sequence starting at 0.012 $M_\odot$ (12 M_J). A deuterium main sequence is obtained when the luminosity of the object is entirely provided by the burning of deuterium.

We have updated and expanded upon GG73 in several ways. First, the initial deuterium abundance for our objects, which is taken to be the protosolar value, is D/H = 2×10^{-5}, while GG73 chose D/H = 1.9×10^{-4}, which is the (enriched) terrestrial ratio of deuterium to hydrogen. Second, GG73 did not carry their calculations below $T_{\rm eff}$ = 1260 K, while our interpolation relation (§ 2.1) permits us an essentially unlimited range of $T_{\rm eff}$. Third, our equation of state includes extensive treatment of nonideal behavior, and is quantitatively applicable to all masses in the range from 0.3 to 15 M_J and higher. Finally, GG73 calculated thermonuclear reaction rates for ^{2}D$(p, \gamma)^3$He, taking ion screening into account but not considering electron screening. In such low-mass objects, partially degenerate electrons in metallic hydrogen effectively shield the protons and deuterons, making it easier for them to overcome their mutual Coulomb barrier.

The global enhancement factor exp $[H(0)]$ thus includes ionic and electronic contributions. The quantity $H(0)$, for reactions between the two charges Z_1 and Z_2, is exactly equal to the difference between the excess (nonideal) free energies $F^{\rm ex}$ in the plasma before and after the reaction (Jancovici 1977):

$$H(0) = F^{\rm ex}(\Gamma_1, Z_1; \Gamma_e, r_s) + F^{\rm ex}(\Gamma_2, Z_2; \Gamma_e, r_s) - F^{\rm ex}(\Gamma_{12}, Z_{12}; \Gamma_e, r_s) , \quad (9)$$

where $\Gamma_i = \Gamma_e Z_i^{5/3}$ is the ionic coupling parameter for the ion of charge Z_i, and $Z_{ij} = Z_i + Z_j$ is the charge of the fused pair. The electronic coupling parameter is

$$\Gamma_e = e^2/a_e k_{\rm B} T , \quad (10)$$

and the coupling parameter of the quantum electrons is

$$r_s = a_e/a_0 , \quad (11)$$

where e is the charge of the electron, a_e is the mean inter-electron spacing ($4\pi a_e^3/3 = n_e^{-1}$), $k_{\rm B}$ is the Boltzmann constant, and a_0 is the Bohr radius. The ionic contribution is obtained directly from equation (9) with the most recently determined fits for the OCP free energy (DeWitt, Chabrier, & Slattery 1995). The electronic contribution has been calculated using a polarization potential, i.e., the difference between the bare Coulomb potential and the screened Coulomb potential, which takes into account the aforementioned electron polarization in the interionic potential through the electron dielectric function (Chabrier 1990),

$$V_{ij}^{\rm pol}(r) = \frac{Z_i Z_j e^2}{2\pi^2} \int \frac{1}{k^2} \left[\frac{1}{\epsilon(k, r_s, T)} - 1 \right] \exp\,(i\boldsymbol{k} \cdot \boldsymbol{r}) d\boldsymbol{k} . \quad (12)$$

Here $\epsilon(k, r_s, T)$ is the electron dielectric function as a function of spatial wavenumber k, electron coupling parameter r_s, and (finite) temperature T, which takes into account the electron-electron correlations beyond the RPA approximation, through the so-called local field correction.

Equation (9) relies on the so-called linear-mixing rule, where the free energy of the mixture is given by the linear interpolation of the free energies of the pure components. The accuracy of this approximation was demonstrated initially for the bare Coulomb potential (Brami, Hansen, & Joly 1979) and has been verified for the screened Coulomb potential (Chabrier & Ashcroft 1990).

A complete presentation of the present formalism, and its application to the nuclear reactions of light elements in low-mass stars, will be given in a forthcoming paper (Chabrier 1995).

3. STRUCTURE AND EVOLUTION

3.1. *The Deuterium-burning Phase*

Several models straddling the limiting mass of deuterium burning are presented in Figure 2. Figure 2*a* shows the luminosity as a function of time, for models with masses from 10–15 $M_{\rm J}$ in steps of 1 $M_{\rm J}$ (masses increase upward). The filled circle is the lowest mass (12 $M_{\rm J}$) model of GG73, during the phase on the deuterium-burning main sequence which GG73 find for an elevated D/H value. Figure 2*b* shows f_N, the fraction of the luminosity derived from $^2D(p, \gamma)^3$He. The deuterium main sequence is defined by $f_N = 1$. In Figure 2, the solid curves are calculated with the full thermonuclear screening corrections, while the dotted curves are calculated with the older ion-only screening corrections. The electron screening theory takes into account electrons at finite temperature, but the effect of thermal corrections to the electron distribution is very slight and a $T = 0$ theory for electron screening appears to be adequate. The heavier curves in Figure 2 show the transitional model of 13 $M_{\rm J}$, in which D/H declines from an initial value of 2×10^{-5} to a final value of 1.5×10^{-5}. For comparison, with ion-only

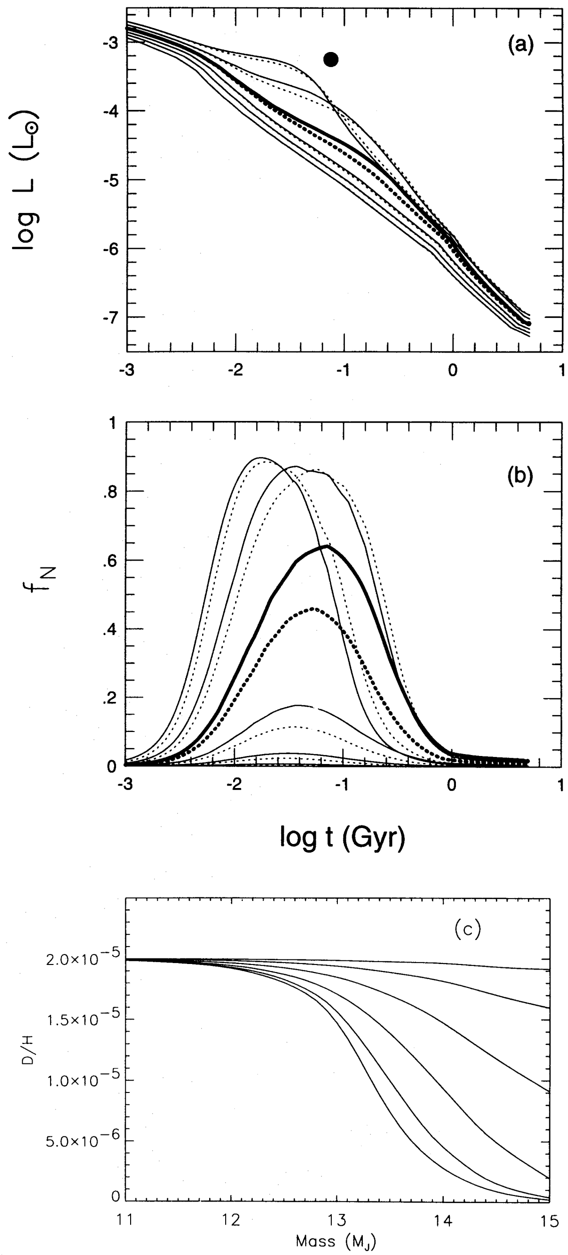

FIG. 2.—(*a*) Luminosity vs. time for masses 10, 11, 12, 13, 14, and 15 $M_{\rm J}$ (*bottom to top*). The 14 $M_{\rm J}$ model ignites deuterium later than the 15 $M_{\rm J}$ model and thus has a higher luminosity from about 0.1 to 1 Gyr. The heavier curves show the 13 $M_{\rm J}$ model, a transition object which barely ignites deuterium. Solid curves show results when full (ion+electron) screening of the nuclear reaction is taken into account. Dotted curves show results when electron screening is neglected. The filled circle shows the low-luminosity end of the deuterium main sequence, computed by GPGO (see text). (*b*) Fraction of luminosity is due to deuterium fusion, f_N, on the same timescale as in (*a*). Because f_N never reaches unity, there is no main sequence. (*c*) Deuterium abundance as a function of mass for log t = 6.74, 7.11, 7.48, 7.85, 8.22, and 9.70 (*top to bottom*).

screening, the final deuterium abundance in the 13 M_J model is 1.7×10^{-5}.

Figure 2*c* shows curves of D/H versus mass for various times, with the final values of D/H evaluated at an age of 5 Gyr. With the best physics included, the mass for which the initial deuterium abundance is ultimately reduced by a factor of 2 is found to be 13.3 M_J. If electron screening is neglected in the calculation of thermonuclear reaction rates, this mass rises to 13.6 M_J.

Despite major differences with the study of GG73, our mass limit for deuterium burning is very similar to theirs. But because we assume an initial deuterium abundance about 1 order of magnitude lower than the terrestrial value, we do not obtain a deuterium main sequence (defined to be a phase where $f_N = 1$).

We conclude that objects with masses below about 12 M_J should retain essentially their entire initial complement of deuterium and derive no luminosity at any stage in their evolution from thermonuclear fusion. Thus, the mass 12 M_J represents a useful boundary to distinguish giant planets from brown dwarfs. Boss (1986) found that the minimum mass for protostars formed from collapse and fragmentation of Population I interstellar clouds was about 20 M_J. Lower mass objects would have to form with the assistance of dense rock-ice cores, and thus would be considered giant planets. It is a coincidence that the limiting mass for giant planets defined by Boss's criterion and that defined by deuterium burning are nearly the same. However, we point out that the deuterium-burning criterion may prove to be the more useful of the two, since it can in principle be applied to observational data in an almost model-independent way. The calculation of the limiting mass for deuterium burning has proved to be very robust over two decades of improvement in the theory.

3.2. *Inflation of Objects by the Central Star*

As is well known (Hubbard 1977), the effect of photons from a primary star thermalized well below an EGPs photosphere is to modify the surface condition and direct the time evolution of the EGP toward an asymptotic effective temperature, set only by the thermalized photons. An EGP with a companion star does not cool to zero temperature but tends toward an equilibrium temperature given by

$$T_{\rm eq} = \left[\frac{(1-A)L_*}{16\pi\sigma a^2}\right]^{1/4} , \qquad (13)$$

where A is the Bond albedo, L_* is the stellar luminosity, σ is the Stefan-Boltzmann constant, and a is the distance between the planet and the parent star.

Because thermal effects on the equation of state are significant for the lighter EGPs, the latter can also reach asymptotic radii significantly larger than that dictated by the zero-temperature equation of state. An EGP orbiting a luminous star will have a larger radius and higher luminosity than would be the case for an isolated EGP, which tends to offset the increased difficulty of detecting it against the greater background signal.

First, for isolated EGPs, Figures 3 and 4 show surfaces of luminosity L and radius R, respectively, as a function of time t and mass M. These surfaces are terminated at a time $t = 5$ Gyr. The "ripple" in luminosity and radius at early times and for masses greater than 12 M_J is caused by deuterium burning, as has been already discussed. Radii decline monotonically with time but show a more complicated behavior with mass. A radius minimum at early times transforms to a very broad maximum at about 4 M_J for late times ($t > 1$ Gyr), and at late times radii are close to the mean radius of Jupiter, 70,000 km. We have plotted the observed values of L and R for Jupiter and Saturn in Figures 3 and 4, respectively. These values differ somewhat from our models for solar composition EGPs for two reasons. The observed values of L for Jupiter and Saturn [$\log (L/L_\odot) = -9.062 \pm 0.034$ and -9.651 ± 0.030, respectively] lie above the models at $t = 4.57$ Gyr because the models are calculated for isolated EGPs, while thermalized photons from a G2 V star are important for both Jupiter and Saturn (Conrath, Hanel, & Samuelson 1989). Furthermore, in the case of Saturn, a significant contribution to L is possibly derived from the immiscibility of helium and metallic hydrogen mixtures (Salpeter 1973; Stevenson & Salpeter 1977a, b; Hubbard & Stevenson 1984; Guillot et al. 1995), which is not included in our EGP models. Finally, it is well known that both Jupiter and Saturn possess dense cores composed of heavy elements, and that the Z-fraction of their mass is enhanced by roughly

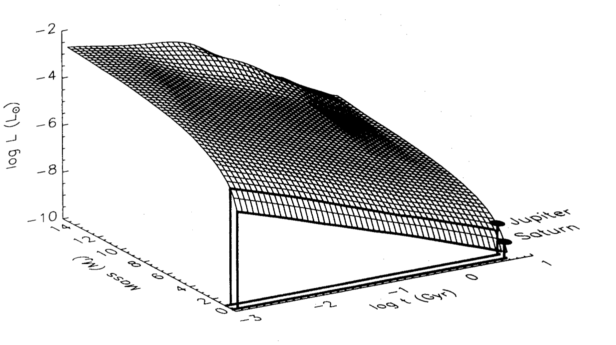

FIG. 3*a*

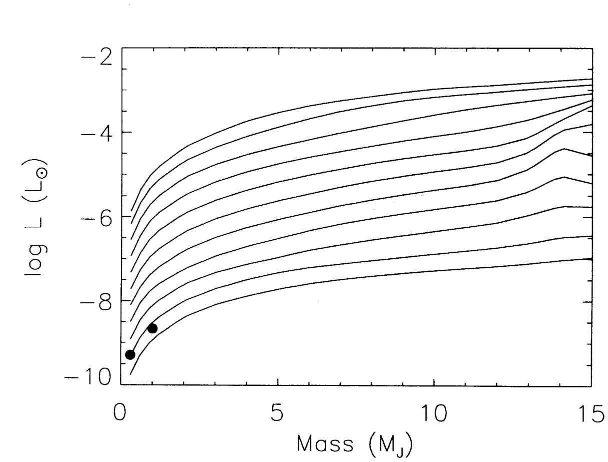

FIG. 3*b*

FIG. 3.—(*a*) Surface of L vs. t and M for isolated EGPs. The surface is terminated at $t = 5$ Gyr. Constant-mass contours for Jupiter and Saturn are highlighted, and observed values are plotted. (*b*) Projection of the surface onto the L vs. M plane, with isochrones for $\log t$ = 6.07, 6.37, 6.74, 7.11, 7.48, 7.85, 8.22, 8.59, 8.96, 9.33, and 9.70 (*top to bottom*), along with observed values for Jupiter and Saturn.

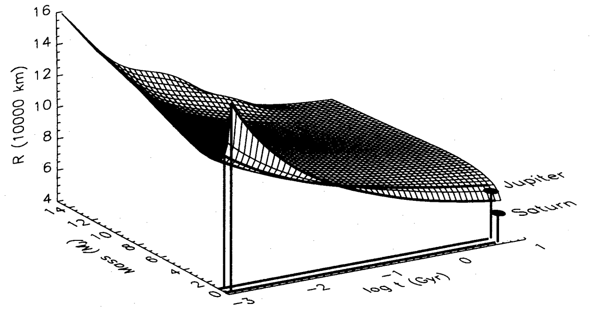

FIG. 4a

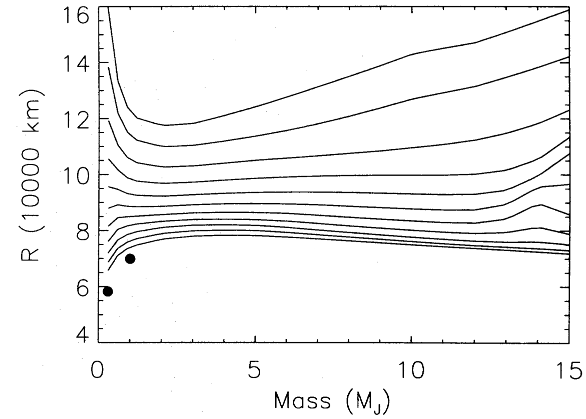

FIG. 4b

FIG. 4.—(*a*) Surface of R vs. t and M for isolated EGPs. The surface is terminated at $t = 5$ Gyr. Constant-mass contours for Jupiter and Saturn are highlighted, and observed values are plotted. The expansion of radii for low masses and early times is a consequence of the polytropic properties of fully convective hydrogen-helium spheres at relatively high entropy. (*b*) Projection of the surface into the R vs. M plane, with isochrones for log t = 6.07, 6.37, 6.74, 7.11, 7.48, 7.85, 8.22, 8.59, 8.96, 9.33, and 9.70 (*top to bottom*), along with observed values for Jupiter and Saturn.

an order of magnitude over solar. It is this phenomenon, partly compensated by expansion because of rotation, that causes the mean radii of Jupiter and Saturn to plot about 3000 and 6000 km, respectively, or about 4% and 10%, below the radii for solar composition EGPs (Fig. 4). The sensitivity of R and L to several of the modeling assumptions is discussed in detail in § 3.3.

To illustrate the pronounced effect of a luminous primary, Figures 5 and 6 show the evolution of EGPs placed 10 AU from an A0 V star. These surfaces are plotted on the same scale as Figures 3 and 4, but are truncated at approximately the main-sequence lifetime of the A0 star ($\sim$0.5 Gyr). Behavior of the more massive EGPs is indistinguishable from Figures 3 and 4, but for objects close to the mass of Jupiter and at late times, the effect of the thermalized photons is dominant and changes the evolution substantially. The lowest mass EGPs ($\sim$1 M_J) reach an asymptotic luminosity about 30 times higher than Jupiter's and their final radii stabilize at about 80,000–90,000 km. There seems to be no problem with the stability of such inflated objects against mass loss; the ratio of their radius to atmospheric scale height is always greater than 1000.

Our theory works quite well for Jupiter after an allowance is made for the modest inflation from a G2 star 5.2 AU distant (Burrows et al. 1995). In the case of Saturn, the larger discrepancies between our EGP model and observed parameters illustrate the increasing effect of nonsolar composition, as well as the possible immiscibility of hydrogen-helium mixtures. Furthermore, as Figure 6*b* makes clear, low-mass EGPs in the vicinity of luminous primaries will be greatly distended. In such an environment, EGPs with radii well in excess of 100,000 km may be found, particularly if they can form with masses below Saturn's mass ($M = 0.3$ M_J). However, the existence of such objects will depend upon whether they can form in an initially gravitationally bound configuration.

3.3. *Effects of Rotation, Helium Abundance, and a Dense Core*

The models presented assume a helium mass fraction $Y = 0.25$, no rotation, and no internal core consisting of heavy elements. On the other hand, we know that Jupiter and Saturn rotate rapidly and possess dense, central cores which are probably formed from refractory materials from the protosolar nebula. Furthermore, we expect the composition of EGPs to differ from our assumed value of $Y = 0.25$. Using the method described in Guillot & Morel (1995) for the integration of the hydrostatic equilibrium in

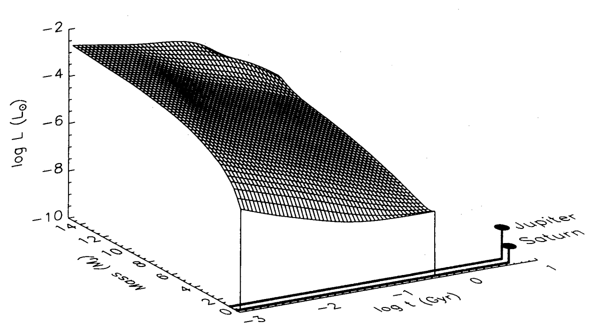

FIG. 5a

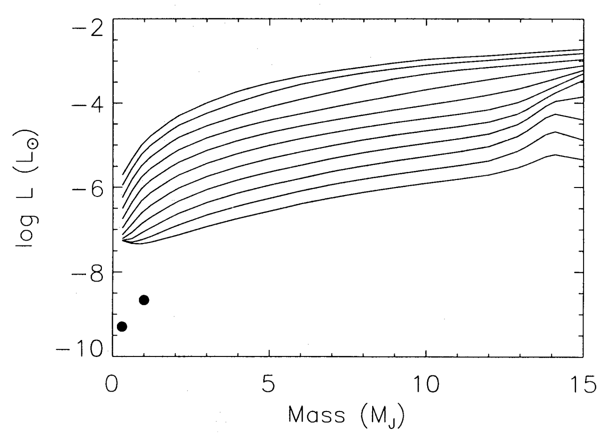

FIG. 5b

FIG. 5.—(*a*) Surface of L vs. t and M for EGPs orbiting a main-sequence A0 star at 10 AU. The surface is terminated at $t = 0.5$ Gyr. Observed values for Jupiter and Saturn are plotted. (*b*) Projection of the surface onto the L vs. M plane, with isochrones for log t = 6.05, 6.27, 6.53, 6.80, 7.07, 7.33, 7.60, 7.87, 8.14, 8.40, and 8.67 (*top to bottom*), along with observed values for Jupiter and Saturn.

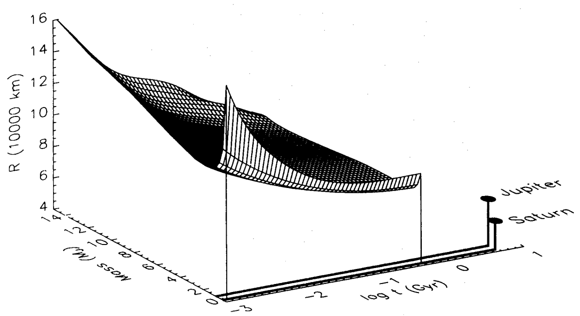

FIG. 6*a*

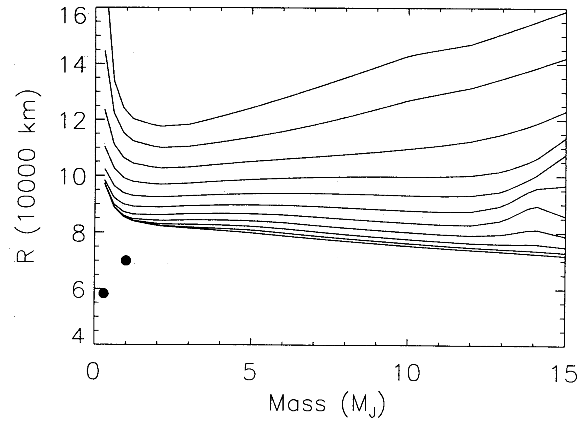

FIG. 6*b*

FIG. 6.—(*a*) Surface of *R* vs. *t* and *M* for EGPs orbiting a main-sequence A0 star at 10 AU. The surface is terminated at $t = 0.5$ Gyr. Observed values for Jupiter and Saturn are plotted. (*b*) Projection of the surface onto the *R* vs. *M* plane, with isochrones for log t = 6.05, 6.27, 6.53, 6.80, 7.07, 7.33, 7.60, 7.87, 8.14, 8.40, and 8.67 (*top to bottom*), along with observed values for Jupiter and Saturn.

the presence of an "ice" + "rock" core, and assuming conservation of the angular momentum of the planet $\mathscr{M}_\omega$ during the evolution, we have investigated the influence of these parameters on the structure of EGPs of 1 and 5 M_J located 5.2 AU from a G2 V star. Our results are depicted in Figures 7 and 8, respectively. In these figures, we measure angular momentum in units of Jupiter's rotational angular momentum, $\mathscr{M}_{\omega,J}$, and the core mass is in units of the Earth's mass, $M_\oplus$.

As expected, the radius decreases as the abundance of helium, *Y*, and the mass of the core, $M_{\rm core}$, increase, and it increases for a planet with a larger angular momentum. Quantitatively, the relative variations of the radius are almost independent of the age of the planet. However, the variations of the luminosity (excluding reflected starlight) shown in Figures 7 and 8 are more complex. Simple analytical models demonstrate that, without stellar insolation, the cooling of a hydrogen-helium object following an evolutionary path defined by $T_{10} \propto T_{\rm eff}^a$ with $a > 0$ is faster for larger radii (Hubbard 1977; Guillot et al. 1995). Inversely, for a given age, the luminosity *increases* with decreasing radius (see the variations of *L* with *Y* and $\mathscr{M}_\omega$ at 0.1 and 1 Gyr, in Figs. 7 and 8). When the effect of stellar insolation becomes significant (at about 4.5 Gyr), the reverse can be true, i.e., an object with a larger radius will receive more energy from the parent star and can then be *more* luminous. On the other hand, Figures 7 and 8 show that the presence of a core tends to decrease the luminosity of the planet in spite of its slightly smaller radius. This effect is due to the reduced heat capacity of the planet.

For a realistic range of helium abundances, rotation rates, and core masses ($Y = 0.2$–0.3, $\mathscr{M}_\omega \leq \mathscr{M}_{\omega,J}$ for 1 M_J EGPs and $\mathscr{M}_\omega \leq 10\ \mathscr{M}_{\omega,J}$ for 5 M_J EGPs, $M_{\rm core} < 20\ M_\oplus$), we expect the variations of the radius and luminosity to be less than 5% at any age. Rapidly rotating EGPs cool faster and are more difficult to detect in the infrared, except when most of their luminosity is due to the energy absorbed from the parent star. Interestingly, planets with a larger abundance of helium are significantly brighter and therefore more easily detectable in the infrared (a more consistent calculation would include the effect of helium abundance on the atmospheric properties, but since the atmospheric absorption is not very sensitive to the helium abundance, this effect is small, at least for $Y < 0.4$). When observing the light *reflected* by EGPs in the visible, the opposite is true; with their smaller radius, planets with high *Y* are more difficult to detect, whereas rapid rotators can be significantly brighter.

There are other effects which can cause departures from the assumed adiabatic interior profiles, such as a first-order phase transition, a radiative zone, the condensation of chemical species, or a phase separation. The effect of the presence of a first-order transition of molecular to metallic hydrogen has been investigated by Saumon et al. (1992) for Saturn, Jupiter, and brown dwarfs, and is found to be small. An increase of the intrinsic luminosity of only about a few percent is expected from the presence of the so-called plasma phase transition. The presence of a radiative region has more of an effect on planetary evolution. As studied for Saturn and Jupiter by Guillot et al. (1995), a radiative zone reduces the luminosity at a given age by about 15%–20% at a given age in Jupiter-like objects. More massive objects are expected to be less influenced by this effect, as the increased absorption due to molecules like H_2O or TiO at higher effective temperatures favors convective over radiative energy transport. The effect of condensation is twofold. First, it can lead to the presence of highly absorbing grains in the atmosphere and, therefore, change its properties. Second, it can affect the temperature profile and thus the internal structure of the planet. Unfortunately, these effects cannot be quantified without further studies. A phase separation of helium in hydrogen is postulated in Saturn in order to explain its high luminosity (Stevenson & Salpeter 1977b), and it is also possible in Jupiter (Guillot et al. 1995). Helium-hydrogen separation will yield smaller atmospheric helium abundances and higher luminosities. However, this occurs only in objects that are cold enough, i.e., relatively low mass and old objects. The relative agreement between evolution models of Jupiter and the age of the solar system tells us that, in planets of the size of Jupiter or larger, and at $t < 4.5$ Gyr, the relative increase of luminosity due to a possible phase separation of helium in hydrogen does not exceed 10%.

4. SPECTRAL EMISSION OF EXTRASOLAR GIANT PLANETS

To the best of our knowledge, there has been no work on the atmospheres and synthetic spectra of gaseous objects

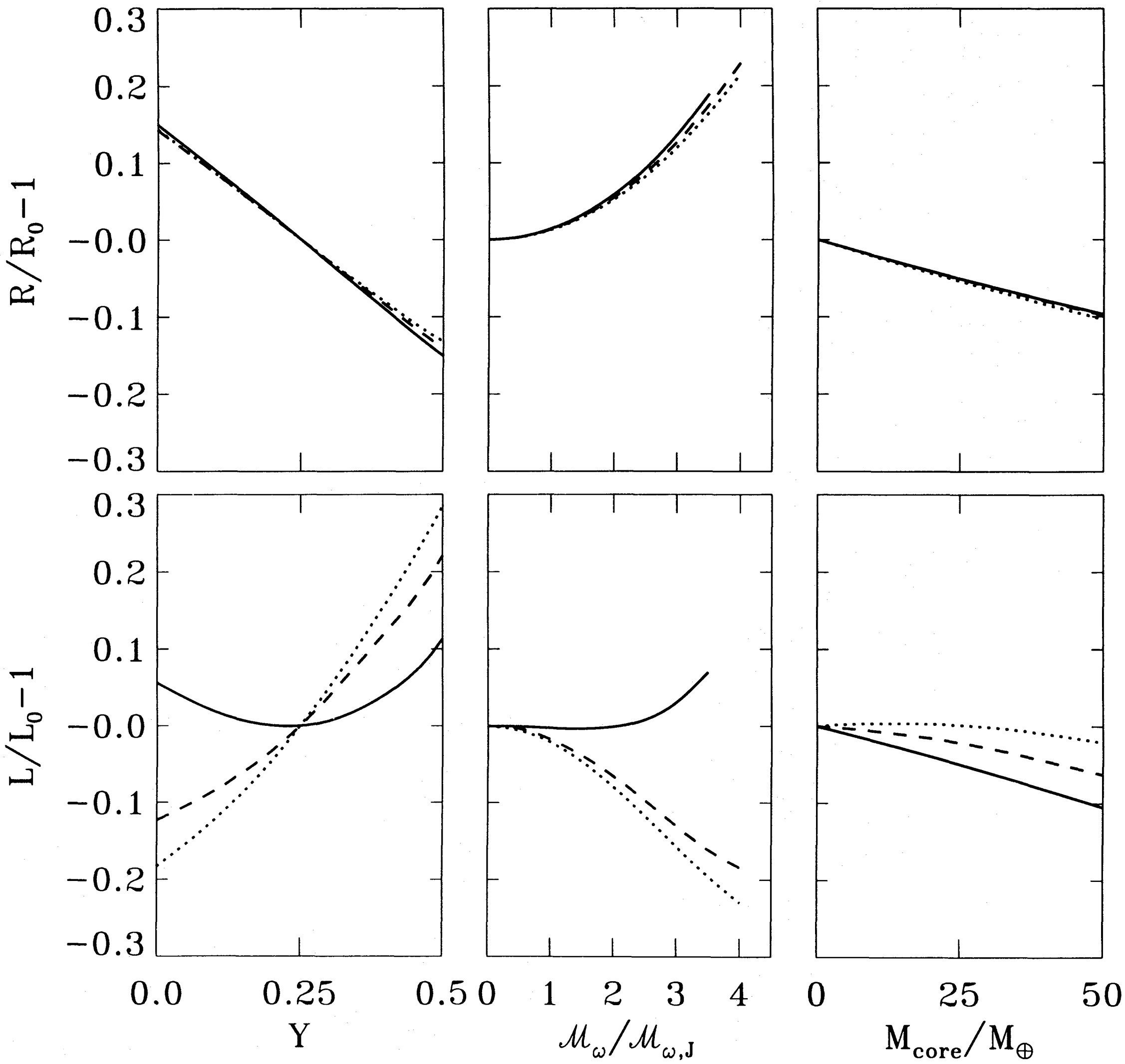

FIG. 7.—Variations of the radius R and total luminosity L (excluding the reflected starlight) of a 1 M_J (or ~318 $M_\oplus$) EGP at 5.2 AU from a G2 V star with the helium mass fraction Y, the angular momentum $\mathcal{M}_\omega$ (in units of the Jovian angular momentum $\mathcal{M}_{\omega,J}$), and the mass of a "rock"+"ice" core M_{core} (in units of Earth masses $M_\oplus$). The EGP's radius and luminosity are compared to a standard model with $Y = 0.25$, no rotation, and no core, of radius R_0 and luminosity L_0. Different ages are represented: 0.1 Gyr (*dotted lines*), 1 Gyr (*dashed lines*), and 4.5 Gyr (*solid lines*). Note that an EGP with $Y = 1$ would be, at 4.5 Gyr, ~2.5 times brighter than our standard model (its *intrinsic* luminosity would be ~6.4 times larger). In models such that $\mathcal{M}_\omega > 3.5\mathcal{M}_{\omega,J}$, the centrifugal acceleration eventually becomes larger than the gravity during the contraction of the planet. Guillot et al. (1994) determine that the mass of the core is about 7 $M_\oplus$ in Jupiter and between 0–20 $M_\oplus$ in Saturn.

with effective temperatures of several hundred degrees, which are typical of young and massive EGPs. The frequency dependence of the albedo and the phase function of such objects are therefore unknown, as are the characteristics of the emitted spectra. While the giant planets of the solar system can be helpful guides at the low-T_{eff} limit of our calculation, the range demonstrated by their spectra serves as a warning against simple generalizations.

Given the trajectories for $L(M, t)$ and $R(M, t)$ presented in § 3.2, approximate spectra for extrasolar giant planets can be generated easily. For lack of a better theory, we have assumed that the EGPs reflect the light of the parent star like a graybody and that the thermal emission is that of a blackbody. These approximations are adequate for the purpose of this calculation, which is to aid in designing search strategies and technological development for the detection of gas giants around nearby stars. A comparison with the actual spectrum of Jupiter is presented below.

The flux from an EGP is the sum of two separate contributions: intrinsic thermal emission (in the infrared) and reflected starlight (in the visible). Following the standard definitions (Mihalas 1978), the flux $\mathcal{F}_\nu$ received at the Earth from an EGP of radius R, orbiting at a distance a from a star of radius R_*, is given by

$$\mathcal{F}_\nu = \left(\frac{R}{d}\right)^2 \mathcal{F}_\nu^p + \frac{A}{4} P(\theta, \phi)\left(\frac{R_*}{d}\right)^2\left(\frac{R}{a}\right)^2 \mathcal{F}_\nu^* , \quad (14)$$

where $\mathcal{F}_\nu^*$ is the flux radiated by the surface of the star, $\mathcal{F}_\nu^p = \pi B_\nu(T_{eff})$ is the thermal flux radiated by the surface of the planet, and d is the distance of the system from the Earth. The Bond albedo is A, and $P(\theta, \phi)$ is the function which accounts for the angular dependence of the reflected light [$\int P(\theta, \phi) d\Omega = 4\pi$], where θ is the star-EGP-Earth angle. $P(\theta, \phi)$ can be measured for solar system objects or computed from the theory of planetary atmospheres. Here we assume the idealized case where the light reflected by the planet is redistributed uniformly over 4π sr or $P(\theta, \phi) = 1$. While $P = 3.2$ for Jupiter in full phase ($\theta = 0$), we estimate that $P \approx 1$ for the quarter phase ($\theta = \pi/2$). This is the

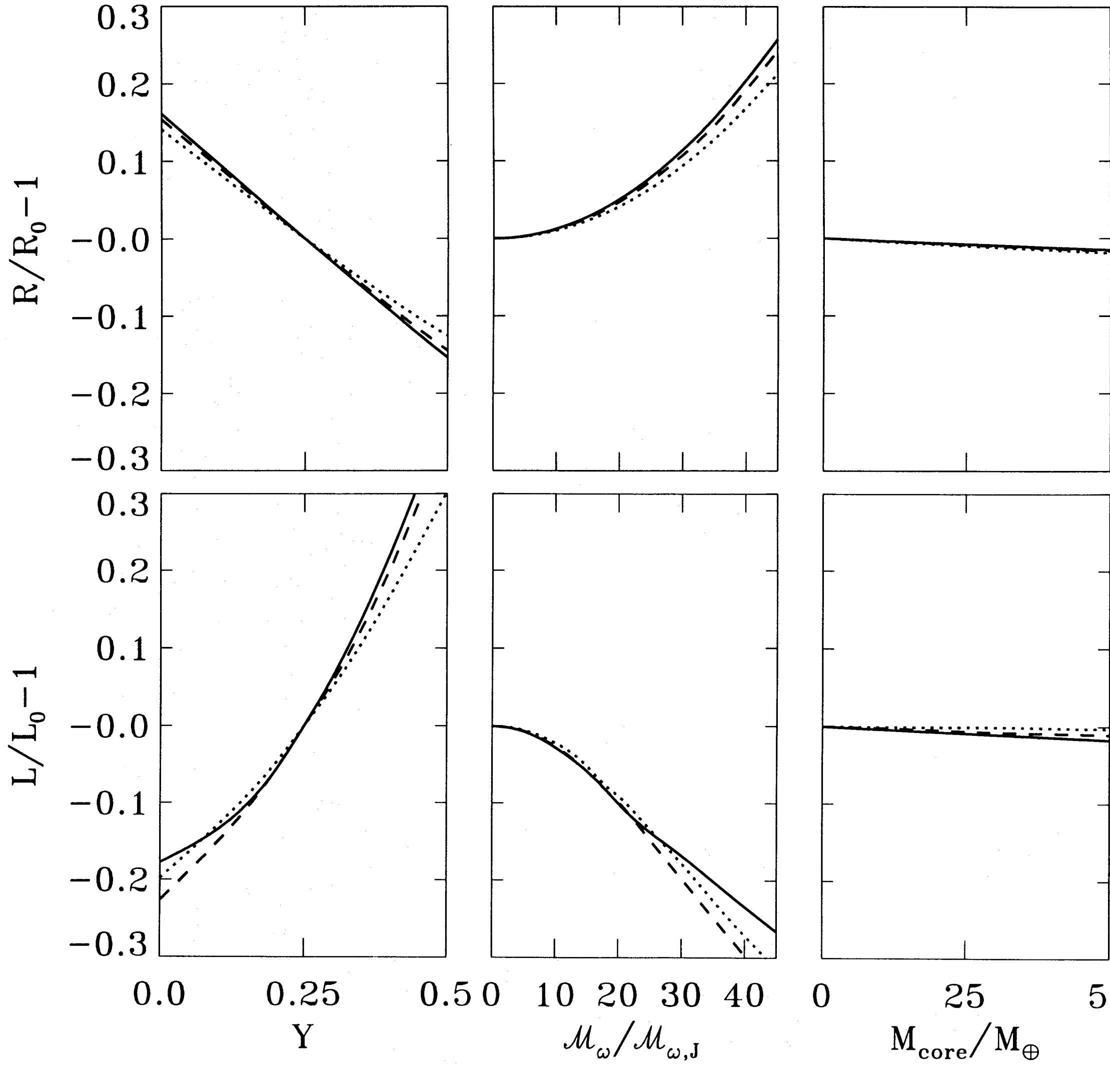

FIG. 8.—Same as Fig. 7, but for a 5 M_J EGP. In this case, the insolation by the central star is less important, as the internal heat flux of the planet itself is much larger. With $Y = 1$, a 5 M_J EGP is (after 4.5 Gyr), ~2.8 times brigher than the same EGP with $Y = 0.25$.

geometry which maximizes angular separation ($\theta = \pi/2$) between the EGP and its central star. If the global scattering properties of the atmospheres of EGPs do not differ dramatically from those of the giant planets of the solar system, our choice of $P = 1$ is representative of the most favorable phase for discovery.

In the next section, we estimate the anticipated deviations of the spectrum of EGPs from a blackbody spectrum. Section 4.2 presents the calculated fluxes from EGPs orbiting stars of spectral types A0 V, G2 V, and M5 V. The spectra $\mathscr{F}_\nu^*$ of the A0 V and G2 V stars are obtained from the model for Vega by Dreiling & Bell (1980) and from the solar irradiance at Earth (A. Eibl 1995, private communication), respectively. Since there are no measured spectra of M5 V stars which cover the wide wavelength range of interest, we use the $T_{\rm eff} = 3100$ K, $\log g = 5.5$ synthetic spectrum of Allard & Hauschildt (1995). These values of $T_{\rm eff}$ and g are based on the main-sequence models of Burrows et al. (1993) and the mass–spectral type relation derived by Kirkpatrick & McCarthy (1994). For stars of other spectral types, $\mathscr{F}_\nu^*$ is taken from the synthetic spectra of Kurucz (1993). These spectra were extended into the far-infrared with blackbody functions as needed.

Figure 9 displays the sensitivity of several ground- and space-based observing platforms which are currently being developed and which will be applied to the search for extrasolar planets. These sensitivities are overlaid on Figures 10–13 and Figure 15, where they can be directly compared with the predicted fluxes from EGPs. Except where noted below, the sensitivities plotted are for the detection of point sources with a signal-to-noise ratio of 5 in a 1 hour integration. In all cases, except for the values at 0.8 μm, the sensitivity is background limited. The sensitivities of the Large Binocular Telescope (LBT) and the upgraded Multiple Mirror Telescope (MMT) at 0.8 μm are based on the application of adaptive optics with the high-order correction scheme proposed by Angel (1994). Diffraction-limited performance is expected from this new technology, which, however, is limited to relatively bright stars ($R \leq 4$). The open triangles, three-pointed stars, and filled triangles show the sensitivities of cameras 1, 2, and 3, respectively, of the Near Infrared Camera and Multiple Object Spectrograph (NICMOS; G. Schneider 1995, private communication), a second-generation instrument for the *Hubble Space Telescope* (*HST*). The integration time is limited to 40 minutes, as imposed by the *HST* orbit. Camera 2 has a 0"3 occulting disk to be used for planet searches. Thin solid lines show the sensitivity of the Infrared Space Observatory (*ISO*;

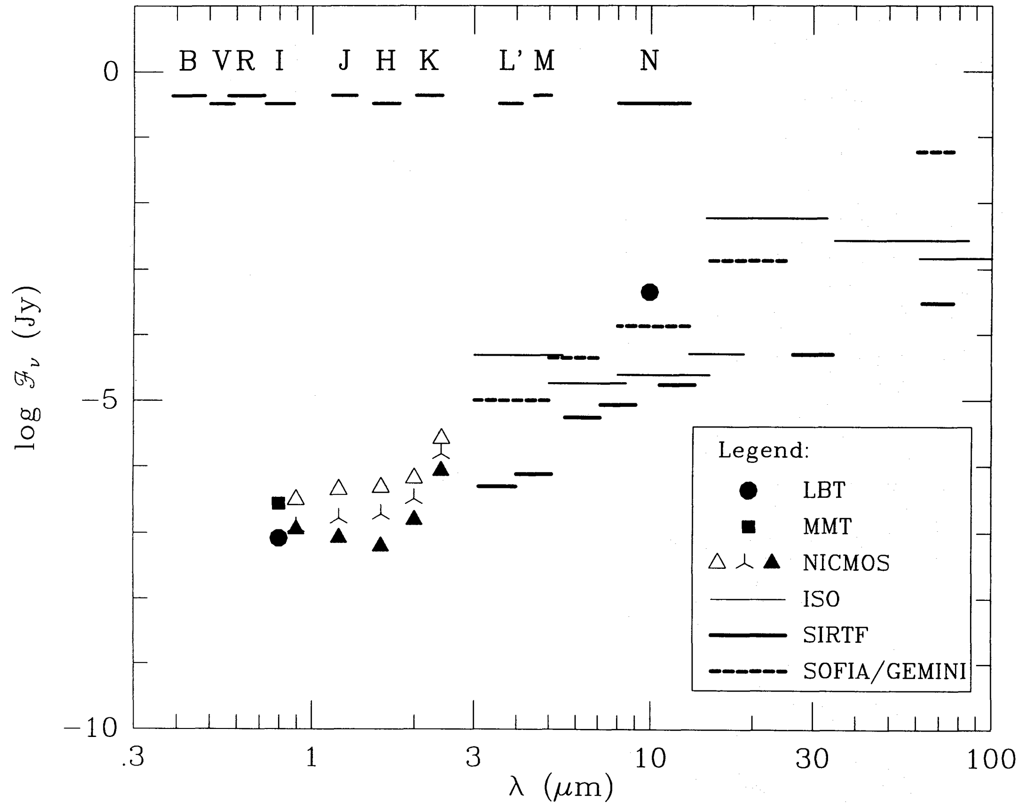

FIG. 9.—Sensitivities of ground-based and space-based observing platforms currently in development which will be applied to the search for extrasolar planets. The values quoted are for a 5 σ detection of a point source in 1 hr of integration, except for the three NICMOS cameras, where the integration is limited to 40 minutes. The 0.8 μm sensitivities of the LBT and MMT depend on the brightness of the primary star. Standard photometric bandpasses are indicated at the top.

ISOCAM Manual 1994; ISOPHOT Manual 1994). The lengths of the lines reflect the filter bandpasses. The Space Infrared Telescope Facilty (SIRTF) is the most sensitive mission currently in development at infrared wavelengths (shown by the thick solid lines; P. Eisenhard 1995, private communication). Under the current design, the resolution at the shortest wavelengths is $\sim 1''$–$2''$. Finally, we also consider the Stratospheric Observatory for Infrared Astronomy (SOFIA) and the infrared capability of the Gemini telescope (*dashed lines*; P. Eisenhardt 1995, private communication). Except for *ISO*, which is built and scheduled for launch in 1995, all sensitivities given here represent the best current estimates at the present stage of development of each mission. A detailed comparison of predicted fluxes with instrumental sensitivities is deferred to § 4.3.

4.1. *Comparison of Jupiter's Spectrum with the Blackbody Approximation*

A comparison between our calculated spectrum for a 1 M_J EGP orbiting a G2 V star at 5.2 AU (assuming blackbody emission) and the observed spectrum of Jupiter is presented in Figure 10. Saturn has a very similar spectrum (e.g., Chamberlain & Hunten 1987; Karkoschka 1994), except that the ammonia absorption is less intense because it condenses at deeper levels. For these planets, the flux can depart from blackbody emission by more than 1 order of magnitude at a given wavelength (e.g., at 2.2, 5, and 6 μm). Almost all features in the Jovian spectrum correspond to molecular absorption bands. Because of the quasi-periodic structure in frequencies of the absorption of molecules such as CH_4, NH_3, and H_2O, these departures average out when using very broad spectroscopic bands (with an extent larger than about 2000 cm^{-1}). However, for practical reasons, observations will generally be constrained to narrower bands. It is therefore interesting to estimate where, for a given EGP, we expect the emitted flux to be higher than that of a blackbody.

The Jovian spectrum is, at large wavelengths ($\lambda \gtrsim 50$ μm), dominated by strong absorption bands of NH_3. Similar absorption bands of NH_3 are present between 8 and 13 μm, 5 and 7 μm, 2.8 and 3.1 μm, 2.2 and 2.4 μm, 1.9 and 2.05 μm, and 1.4 and 1.55 μm. The roto-translational band of collision-induced absorption by molecular hydrogen dominates from 13 to 45 μm, and the first vibrational band is centered on 2.5 μm. Methane has strong absorption bands centered around 7.5, 6, 3.5, 2.5, 1.7, 1.4, 1.15, and 1 μm. Water is buried deep in the Jovian atmosphere, so that it does not have a significant effect on the spectrum of the planet (though water lines are visible in the 5 μm region). For wavelengths between 0.4 and 1 μm, backscattering by ammonia clouds becomes very efficient and the albedo of the planet approaches 0.7 (compared to an average Bond albedo of 0.35). Narrow methane absorption bands are seen near 0.7, 0.9, and 1 μm. Clearly, the most favorable bands for observing Jupiter are between 0.4 and 1 μm, 4.5 and 5.3 μm, and 7 and 13 μm.

EGPs with effective temperatures below 150–200 K (corresponding to 1 M_J objects older than 0.4 Gyr, or 5 Gyr-old EGPs less massive than 5 M_J, orbiting G2 V or later stars) are expected to have spectra similar to that of Jupiter. For higher effective temperatures the absorption by water clouds and water vapor is expected to play a domi-

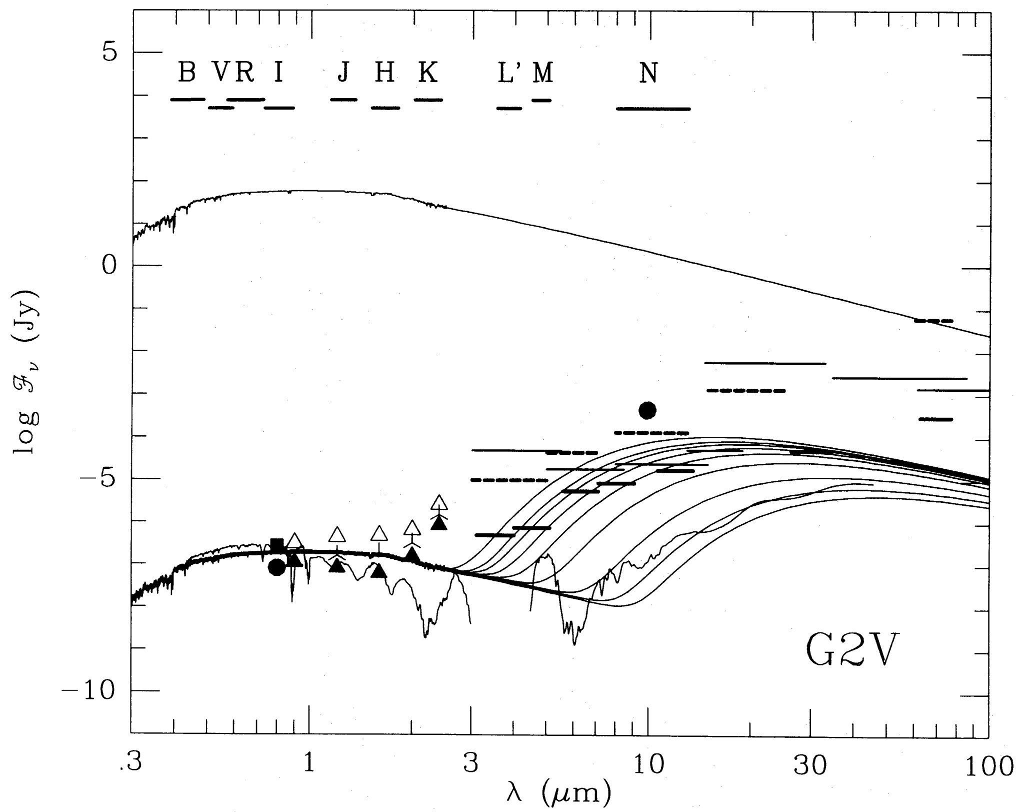

FIG. 10.—Spectral flux for EGPs orbiting at 5.2 AU from a G2 V star at 10 pc from the Earth. Solid curves correspond to the following masses: 0.3, 1, 2, 4, 6, 8, 10, 12, and 14 M_J (the more massive EGP being more luminous) at the age of the solar system, 4.5 Gyr or log $t = 9.653$. A composite spectrum of Jupiter is superposed on the emission of the EGPs (Hanel et al. 1979; Hunten, Tomasko, & Wallace 1980; Karkoschka 1994). The spectrum of the star is shown to scale. Other symbols are the same as in Fig. 9.

nant role in the spectrum. As the most common spectroscopic bands avoid the prominent absorption bands of water, observing in these bands should reveal both "cold" and "hot" EGPs with a comparable efficiency. Note, however, that for hot enough objects, significant changes in the chemical composition (as the transformation of CH_4 to CO) are expected to yield major changes in their emission. Scattering by cloud particles is likely to increase the flux of all EGPs in the *B*, *V*, *R*, and *I* bands. This effect should be even more significant when water condenses at low pressures (i.e., for "hot" EGPs), as seen on Venus, whose albedo is close to 0.9 in the 0.5–2.8 μm region (e.g., Moroz 1983). On the other hand, methane (and possible water) absorption bands strongly reduce the *reflected* flux in the 1–4 μm region, where no backwarming effect (e.g., Mihalas 1978) occurs, except for very hot EGPs. Hence, this spectroscopic region (which includes the *J*, *K*, and *H* bands) is probably less favorable.

From the ground, EGPs with effective temperatures between 200 and 300 K should be observed in the *B*, *V*, *R*, *I*, *L′*, *M*, and *N* bands, where we expect the flux to be maximized. Colder EGPs ($T_{\rm eff} \lesssim 200$ K) should be observed in the *B*, *V*, *R*, *I*, *M*, and *N* bands, near 2.7 μm, and possibly at 1.25 μm (*J* band), and 1.5 μm (*H* band). EGPs in orbit around A0 stars always have effective temperatures above 300 K, even for a semimajor axis of 20 AU. It is therefore very difficult to predict their emissions without a consistent thermochemical calculation. Nonetheless, it is probable that these objects are still dominated by absorption bands of water, and should therefore also be observed in the *B*, *V*, *R*, *I*, *L′ M*, and *N* bands. Evidently, searches for EGPs should be conducted in several bandpasses. From space however, the most favorable region is in the 20–30 μm range.

4.2. *Predicted Fluxes*

The flux received at the Earth from an EGP depends strongly on several parameters: the luminosity of the primary star, L_*; the semimajor axis of the orbit, *a*; the mass of the planet, M_p; its age, *t*; and the distance of the system, *d*. The combinations of these parameters which occur in nature and that will lead to a successful detection of an EGP are not known a priori, but this rather broad parameter space can be somewhat constrained. Most searches are restricted to nearby stars, and we adopt a representative distance of $d = 10$ pc. The nearby star sample has a median age of about 2 Gyr, and it does not contain stars of spectral type earlier than A0. Furthermore, the example provided by the solar system, supplemented by protoplanetary disk models, limits the range of plausible values of *a* within a few AU to a few tens of AU.

In this section we discuss a representative subset of our results. Combinations of primary stars and orbital radii that we consider in detail first include a system analogous to the solar system, with a G2 V star and EGPs orbiting at 5.2 AU (to allow a direct comparison with the familiar case of Jupiter) and at 10 AU. There are 21 G dwarfs within 10 pc (T. Henry 1995, private communication). Four A stars (Vega, Altair, Sirius, and Fomalhaut) occupy the bright end of the local population, and we consider EGPs orbiting at 10 AU and 20 AU from an A0 V star. Finally, the most numerous stars in the solar neighborhood are M dwarfs. As we will see, M dwarfs are so faint that their light contributes little if anything to the thermal emission of EGPs. However, in order to examine a case with significant flux of reflected light, we choose a smaller orbital radius of $a = 2.6$ AU. Tables of fluxes in the V–N bandpasses for selected models are given in the Appendix.

The dependence of the predicted flux on the mass of EGPs in a system analogous to the Sun-Jupiter pair is shown in Figure 10, where the planets are orbiting at 5.2 AU from a G2 V star. The system is placed at 10 pc from the Sun and has the age of the solar system (4.5 Gyr). From left to right, the masses decrease from 14 to 0.3 M_J (the mass of Saturn). The uppermost curve shows the spectrum of the star. Standard photometric bandpasses are indicated at the top of the figure, and other symbols indicate the sensitivities of several instruments (see Fig. 9). After 4.5 Gyr of cooling, these planets have reached their final radius. For the masses considered, the radius of solar composition planets falls in the narrow range of 1.01–1.09 R_J, where R_J is Jupiter's radius. Except in cases of significant inflation (see § 3.2), the radius of the EGP is essentially independent of its mass. It follows that the light reflected by the planet from primaries of type G2 and later is also independent of the mass. This is true in most cases because a broad maximum in the $R(M)$ relation is found around 4 M_J for objects of solar composition, and all EGPs therefore have similar radii. In general, the ratio of the luminosity reflected by the planet to that of the star is fixed by the separation ($\sim a^{-2}$) and is $\sim 3 \times 10^{-9}$ in Figure 10.

On the other hand, the thermal emission of an EGP rises very rapidly with its mass in the 3–15 μm range, which corresponds to the Wien tail of the Planck function. In Figure 10, the analog of the Sun-Jupiter system is given by the 1 M_J curve, which is the second from the right. Just doubling the mass to 2 M_J can increase the flux by an order of magnitude at N, where the contrast between star and planet is reduced to $\sim 10^5$–10^6. At wavelengths above 30 μm, both the stellar and EGP spectra are in the Rayleigh-Jeans limit of the Planck function, and the planet to star flux ratio becomes independent of wavelength;

$$\frac{\mathscr{F}_\nu^p}{\mathscr{F}_\nu^*} = \frac{T_{\rm eff}^p}{T_{\rm eff}^*}\left(\frac{R^2}{R_*^2}\right). \qquad (15)$$

Various combinations of parameters involving a G2 V central star 10 pc away from the Sun are shown in Figure 11. Figure 11*a* shows the evolution of the spectrum of a 1 M_J EGP, orbiting at 5.2 AU. The seven curves shown span ages from 0.01 to 5 Gyr, the rightmost curve corresponding approximately to the present Jupiter. Jupiter was much brighter in the past, with vigorous thermal emission. At 0.1 Gyr, Jupiter was as bright as a 14 M_J EGP at the present age of the solar system (Fig. 10). On the other hand, the reflected light decreases very slowly with time, as EGPs at 5.2 AU from a G2 V star are already within 30%–40% of their final radius at 0.01 Gyr. The decrease in the reflected flux due to the contraction of the planet is less than a factor of 2.

The spectral evolution of a 5 M_J EGP is shown in Figure 11*b*, where all other parameters are identical to those of Figure 11*a*. As depicted in Figure 3*b*, a 5 M_J EGP remains $\sim$10–20 times more luminous than a 1 M_J at all of the times considered here. This translates into infrared fluxes which can be up to 1300 times larger than for a 1 M_J EGP in the K–N bands. For a given age, the highest flux ratios between these two masses are obtained in the band where the lower mass EGP emits only in reflected light, while falling near or blueward of the peak of thermal emission of the more massive EGPs. The emissions of a relatively old 5 M_J EGP at 5 Gyr are nearly identical to those of a much younger 1 M_J at the age of 0.3 Gyr.

Figure 11*c* is similar to Figure 10, but at $t = 1$ Gyr. Masses from 0.3 to 14 M_J are shown. While all EGPs are brighter in this figure than in Figure 10, there is hardly any change for the 0.3 M_J (*rightmost curve*), since it reaches its final equilibrium temperature around 1.6 Gyr. On the other hand, at 1 Gyr the 14 M_J model is still burning deuterium, albeit at a very slow rate. After 5 Gyr, all the deuterium has been consumed (as in Fig. 10).

If the orbital separation is increased, there is a corresponding decrease in the reflected flux ($\sim a^{-2}$), but the thermal flux is not affected until $T_{\rm eff}$ approaches $T_{\rm eq}$. The equilibrium temperature (eq. [13]) decreases with larger a, and the saturation effect on the spectrum occurs later. This is shown for a 0.3 M_J EGP (Saturn's mass) in Figure 11*d*, for $a = 5.2$ AU (*solid lines*) and $a = 10$ AU (*dashed lines*). The curves correspond to different ages ranging from 0.01 to 5 Gyr. For the first 0.1 Gyr of evolution, the thermal emission is dominated by internal heat, and stellar insolation is negligible. The spectrum of the EGP is independent of a during this initial period. An EGP with as low a mass as 0.3 M_J reaches its equilibrium configuration fairly early, in this case after 1.6 Gyr (for $a = 5.2$ AU). There is no further evolution of the EGP, and its spectrum remains unchanged. This can be seen in the set of solid curves, where 3 Gyr and 5 Gyr are superposed. At a distance of 10 AU, $T_{\rm eq}$ is lower and the EGP therefore cools for a longer time (*dashed lines*).

We illustrate the case of the brightest stars in the solar neighborhood by considering an A0 V central star at 10 pc. Such a star has a mass of about 2.8 $M_\odot$, and a rather short main-sequence lifetime of $\sim$0.4 Gyr. Therefore, planetary systems around A stars are young. The four panels of Figure 12 correspond to the panels of Figure 11, with minor differences indicated below. Figures 12*a* and 12*b* show the evolution of 1 and 5 M_J EGPs, respectively, orbiting at 10 AU from the star for ages of 0.01, 0.03, 0.1, 0.2, and 0.4 Gyr. The thermal emission during the early evolution is dominated by internal cooling, and the absorbed heat from the star is negligible. This part of the spectrum is identical to Figures 11*a* and 11*b*. On the other hand, an A0 V star is $\sim$80 times brighter than a G2 V star, and this results in a larger flux of reflected light. The steeper slope of the A0 V spectrum also results in higher fluxes at shorter wavelengths.

The full range of masses considered (0.3–14 M_J) is shown in Figure 12*c* for 0.2 Gyr, midway through the main-sequence life of the A0 V star. At this young age, the 14 M_J EGP is still burning deuterium and emits vigorously in the near-infrared. As discussed in § 3.2, models of lower mass are significantly inflated by the absorbed stellar flux from the bright A star. As a consequence, the thermal emission of the 0.3 M_J model is comparable to that of the 1 M_J model.

The effect of increasing the planet-star separation from 10 AU (*solid lines*) to 20 AU (*dashed lines*) is shown in Figure 12*d*. The spectra correspond to ages of 0.01, 0.03, 0.1, 0.2, and 0.4 Gyr for EGPs of 2 M_J. The effect on the thermal emission is not nearly as pronounced as in Figure 11*d* because of the higher mass of the EGP considered here.

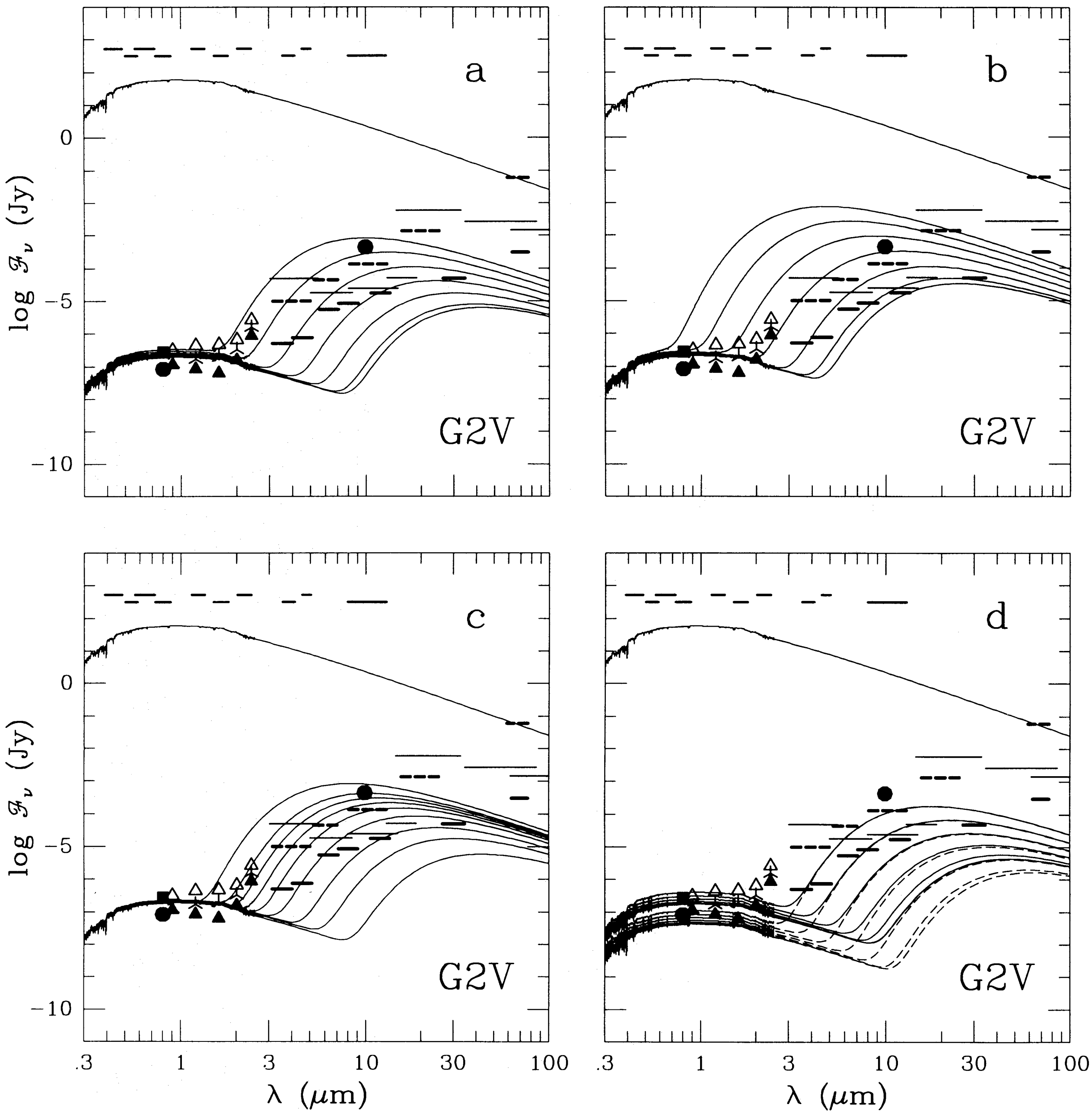

FIG. 11.—Spectral flux for EGPs orbiting a G2 V star at 10 pc from the Earth. (*a*) 1 M_J EGP at 5.2 AU from the central star at ages of log t = 7, 7.5, 8, 8.5, 9, 9.5, and 9.7 (*left to right*). (*b*) Same as (*a*), but for a 5 M_J planet. (*c*) EGPs of masses 0.3, 1, 2, 4, 6, 8, 10, 12, and 14 M_J (*right to left*) orbiting at 5.2 AU and at an age of log t = 9. (*d*) 0.3 M_J planet orbiting at 5.2 AU (*solid lines*) and 10 AU (*dashed lines*) at times of log t = 7, 7.5, 8, 8.5, 9, 9.5, and 9.7 (*left to right*). The spectrum of the star is shown to scale. Other symbols are the same as in Fig. 9.

Internal heat dominates the absorbed stellar flux in the more massive and younger objects. As expected, the reflected light is reduced by a factor of 4 as the distance from the central star is doubled to 20 AU. This ratio would be larger for less massive EGPs, which are inflated by absorbed stellar radiation.

Late M dwarfs represent a substantial pool of candidate stars for planetary system searches, since they are by far the most abundant type of stars in the solar neighborhood. Because they are intrinsically faint, the contrast between star and planet is minimized at infrared wavelengths for late M dwarfs. This is illustrated in Figure 13, which considers EGPs orbiting an M5 V star 10 pc away from the Sun. The luminosity of the star is so low ($L \approx 0.0034\ L_\odot$) that it does not contribute to the energy balance of the EGP. Except for the reflected light, the spectrum of an EGP orbiting an M5 V star is identical to that of an isolated EGP. To exhibit a case of significant reflected light flux, we adopt an orbital radius of 2.6 AU. Using the semi-analytic protoplanetary disk model of Wood and Morfill (1988), and assuming that the disk accretion rate is independent of the mass of the central star and that Jupiter formed at the inner boundary of the zone where water ice condensed in the protosolar nebula, we can scale their disk model to other stars. The distance thus obtained for water ice condensation (2.6 AU for a M5 V star) is more sensitive to the mass of the central star than predicted by the more detailed calculation of Boss (1995). The relatively small a that we derive for a possible EGP companion to an M5 V star gives some basis for searching such late stars for EGP emissions.

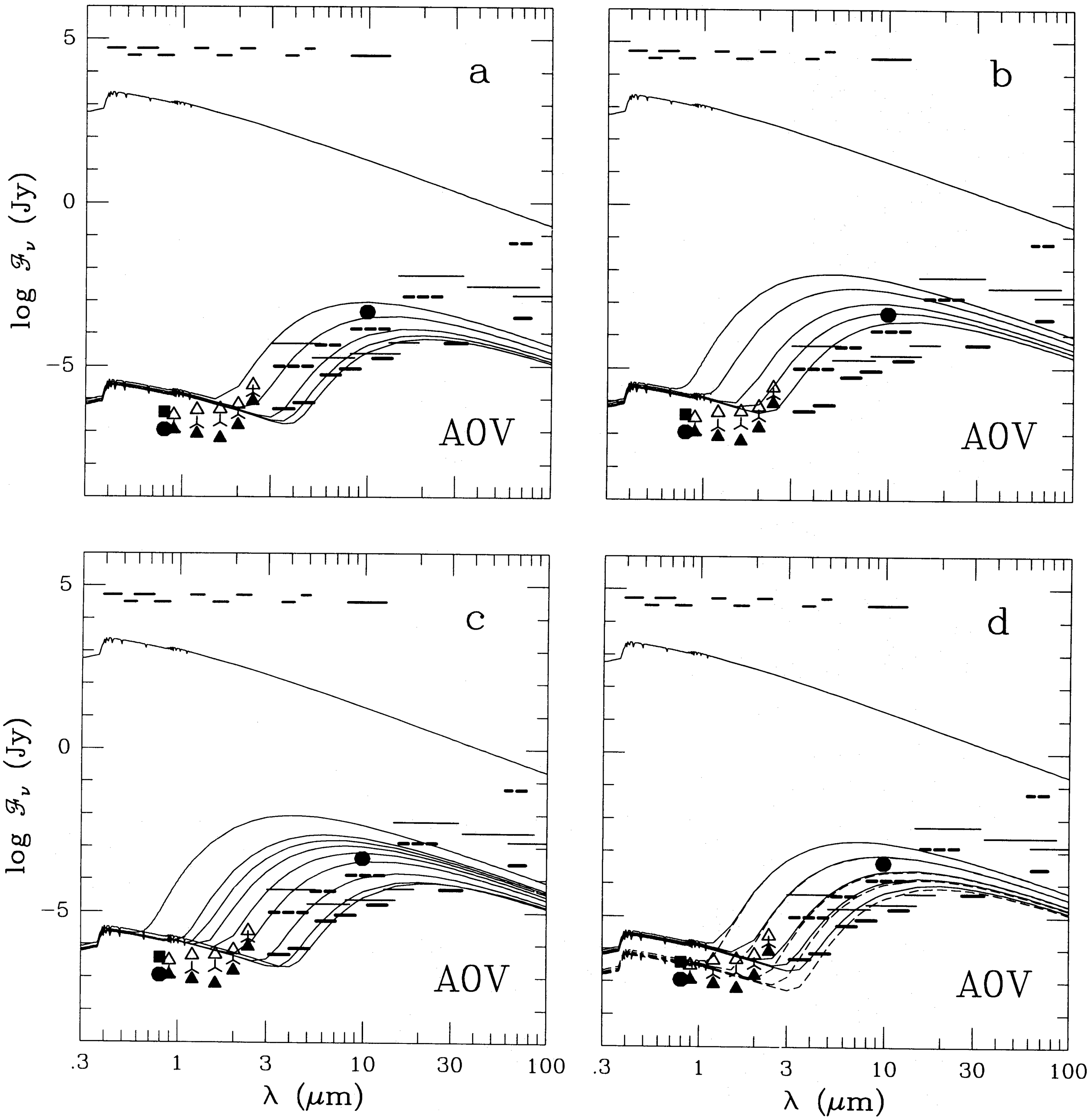

FIG. 12.—Spectral flux for EGPs orbiting an A0 V star at 10 pc from the Earth. (*a*) 1 M_J EGP at 10 AU from the central star at ages of log t = 7, 7.5, 8, 8.3, and 8.6. (*b*) Same as (*a*), but for a 5 M_J planet. (*c*) EGPs of masses 0.3, 1, 2, 4, 6, 8, 10, 12, and 14 M_J orbiting at 10 AU and at an age of log t = 8.3. (*d*) 2 M_J planet orbiting at 10 AU (*solid lines*) and 20 AU (*dashed lines*) at times of log t = 7, 7.5, 8, 8.3, and 8.6. The spectrum of the star is shown to scale. Other symbols are the same as in Fig. 9.

For 0.01 Gyr < t < 1 Gyr, the evolution of the spectrum of a 1 M_J EGP around a M5 V star (Fig. 13*a*) is identical to that around a G2 V star (Fig. 11*a*). The former will cool further to reach $T_{\rm eff} \approx 75$ K after a Hubble time, while the luminosity of the G2 V primary will hold it at $T_{\rm eq} \approx 100$ K. Several curves are shown for the stellar spectrum in Figures 13*a*, 13*b*, and 13*d*, because an M5 V star contracts for about 0.5 Gyr before settling on the main sequence. During this period, its luminosity decreases steadily at a nearly constant $T_{\rm eff}$. In reflected light, this EGP is 1–3 orders of magnitude fainter than its counterpart orbiting a G2 V star. Because a 5 M_J EGP is powered mostly by its internal heat during the period covered here (t < 5 Gyr), its thermal spectrum is identical to that of EGPs orbiting G2 V and A0 V stars. This is shown in Figure 13*b*.

The spectra of EGPs with a range of masses (from 0.3 to 14 M_J), orbiting at 2.6 AU from a 1 Gyr old M5 V star, are shown in Figure 13*c*. Again, except for the reflected light, which is a few orders of magnitude fainter, the spectra are nearly identical to those of Figure 11*c*. In the latter figure, the 0.3 M_J model is twice as bright in thermal emission because of the light absorbed from the G2 V star. Finally, since the light of the M5 V star is so feeble, only the reflected light portion of the spectrum is affected by changing the orbital separation a. This is shown in Figure 13*d* for a 2 M_J EGP orbiting at 2.6 and 5.2 AU for ages of 0.01, 0.03, 0.1, 0.3, 1, 3, and 5 Gyr.

In the Rayleigh-Jeans limit of both the stellar and planetary spectra (in the far-infrared), the flux from a 5 M_J EGP is about 3% of that of the central star, a considerably lower

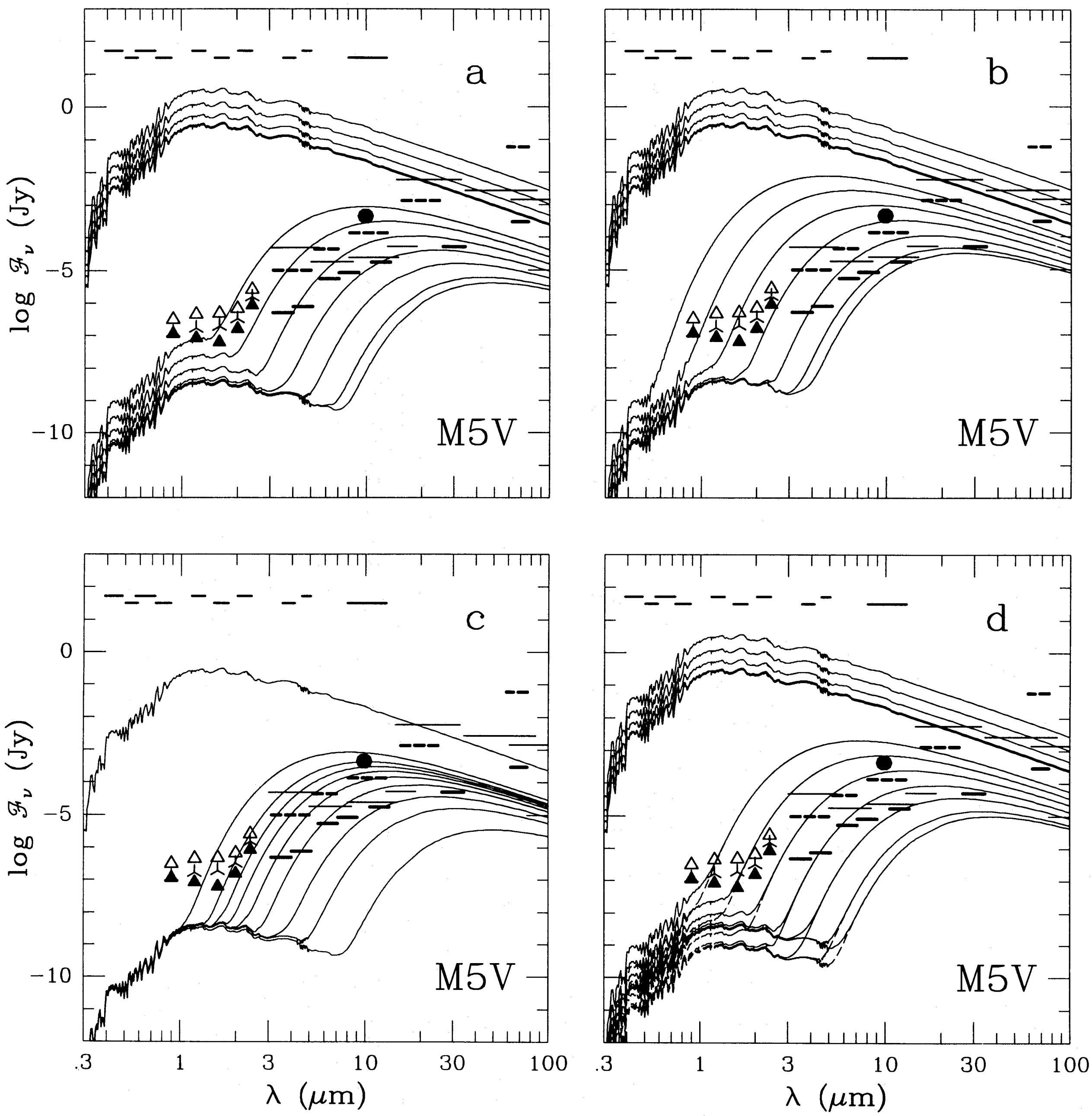

FIG. 13.—Spectral flux for EGPs orbiting a M5 V star at 10 pc from the Earth. (*a*) 1 M_J EGP at 2.6 AU from the central star at ages of log t = 7, 7.5, 8, 8.5, 9, 9.5, and 9.7 (*left to right*). (*b*) Same as (*a*), but for a 5 M_J planet. (*c*) EGPs of masses 0.3, 1, 2, 4, 6, 8, 10, 12, and 14 M_J (*right to left*) orbiting at 2.6 AU and at an age of log t = 9. (*d*) 2 M_J planet orbiting at 2.6 AU (*solid lines*) and 5.2 AU (*dashed lines*) at times of log t = 7, 7.5, 8, 8.5, 9, 9.5, and 9.7 (*left to right*). The spectrum of the star is shown to scale at the top, and the luminosity of the M5 V star decreases as it contracts toward the main sequence. Contraction stops when the ZAMS is reached shortly before log t = 9. Other symbols are the same as in Fig. 9.

contrast than would be the case with G2 V or A0 V primaries. Nevertheless, we do not predict any significant infrared excess in the energy distribution of any main-sequence star which would be due to the thermal emission of a giant planetary companion. Even in a most favorable case of a young system with a massive 10 M_J planet, the flux ratio remains lower than 8%. Figure 14 shows the flux ratio between a 2 M_J EGP and a M5 V star as a function of wavelength.

4.3. *The Potential for Detection*

As discussed in the previous section, the flux from EGPs represents only a small fraction of the flux of the parent star at any wavelength. Therefore, EGPs are not detectable with photometric surveys unless the EGP and the star show substantial differences in their principal spectral features. In principle, photometric and field imaging could detect "free-floating" EGPs, planet-sized bodies which are not bound to a star. This may be an unrealistic approach, however; similar searches for the more massive and much brighter brown dwarfs have shown how difficult it is to find very dim objects, even in the solar neighborhood. In addition, it may also be impossible for such low-mass objects to form outside the environment of a dissipative protoplanetary accretion disk. It is more probable that planetary-mass objects will be found orbiting nearby stars, thereby qualifying as bona fide planets. The most compelling detection will come from resolving the EGP companion from its parent star by directly imaging the system.

Imaging giant planets around nearby stars presents

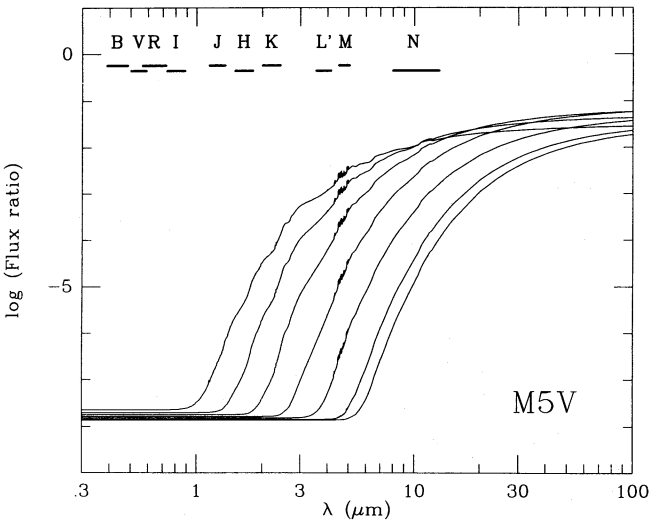

FIG. 14.—Flux ratio between the planet and the primary star for a 2 M_J planet orbiting 2.6 AU from a M5 V star. Curves (*left to right*) are for log t = 7, 7.5, 8, 8.5, 9, 9.5, and 9.7. Standard photometric bandpasses are shown at the top.

major technological challenges. The difficulties arise mainly from the following problems: (1) The brightness ratio between the star and the planet is large and ranges from ~ 30 to 10^9. (2) The small angular separation is perhaps 2″ in a favorable case down to a more typical 0″.5. (3) The flux from the planet is very weak. These three factors stretch the current limits of optical and infrared technologies. Current and next generation instruments are reaching sensitivity levels within the range of the predicted brightnesses of EGPs, but they do not always have sufficiently high angular resolution to resolve the EGP from its parent star. The issue of angular resolution is further complicated by the problem of light scattered in the telescope optics. The point-spread function of diffraction-limited optical systems typically has a very faint halo which can spread over several arcseconds around the Airy disk, due to minute residual errors in the figure of the mirror, light scattered inside the telescope, or residual atmospheric distortions of the images. Because of the enormous contrast between the planet and the primary star, the signal of the planet can be lost in the halo of the primary star. The brightness of this faint halo is very difficult to predict and is expected to vary widely from one instrument to another.

Detection of planets by direct techniques, i.e., imaging using adaptive optics or interferometric techniques, must take into account the scattering of light by dust systems, analogous to our zodiacal light, around candidate stars. Further, such imaging in the mid-infrared is inhibited by our own zodiacal dust, requiring that infrared interferometers be placed in heliocentric orbits at 3 AU or beyond to avoid the worst of the dust emission (R. Angel 1995, private communication). Other star systems which are candidates for planetary searches may have higher dust column densities than our own, and hence more extreme scattering. Backman et al. (1992) constructed dust density profiles for β Pictoris from ground-based photometry in the visual and infrared. Their resulting profiles, even in the region expected to have planets (several to 30 AU), are several orders of magnitude higher than the solar system's zodiacal emission (C. Beichmann 1995, private communication). Happily, the situation is much less severe if searches for giant planets are confined to expected separations of $\gtrsim 5$ AU from the parent star.

Although Saturn is the only planet with a ring system which is both radially broad ($\sim 10^5$ km) and optically thick, all giant planets of the solar system have rings, and we expect them to occur in other planetary systems as well. With favorable geometry, an EGP with a ring system similar to that of Saturn could be a few times brighter in *reflected* light (visible wavelengths). In the thermal infrared, the rings would reemit light absorbed from the central star at their equilibrium temperature, which ranges from ~ 30 to 200 K for plausible systems. In most cases, this is smaller than the effective temperature of the planet and does not contribute much to the overall thermal flux.

The complexity and uncertainty which shroud these issues prevent us from providing a complete discussion of the detectability of EGPs. However, our calculations do predict their brightnesses, and the sensitivity of existing and projected instruments is reasonably well known. In the following discussion, we focus on the sensitivity of a set of representative instruments in the light of predicted EGP fluxes to comment on the detectability of EGPs in the near future. Other aspects of detection are brought into the discussion as deemed appropriate.

The three NICMOS cameras, with resolutions of 0″.043, 0″.075, and 0″.2, respectively, are very promising instruments for the detection of EGPs in the solar neighborhood. They are sensitive in the near-infrared where most EGPs emit in reflected light. Figures 10–13 indicate that NICMOS will be able to detect EGPs around most types of central stars. Since the reflected light is nearly independent of the mass or the age of the planet, a wide variety of systems is within reach of this instrument. The high angular resolution afforded by *HST* should be amply adequate to resolve the systems shown in Figures 10–13, which have an angular separation of 0″.52. The 0″.3 occulting disk of camera 2 should reduce the difficulties associated with the high contrast between the star and the planet. Extrasolar giant planets orbiting M5 V stars are very faint in reflected light, and NICMOS (as well as all other instruments currently in development) is not sensitive enough to be useful. However, Figure 13 shows that in the *J*, *H*, and *K* bandpasses, NICMOS would pick up the thermal emission of the more massive and younger EGPs. A 1 M_J EGP could be detected if it was only 10 Myr (Fig. 13*a*). More massive EGPs stay bright longer, and a 5 M_J EGP could be seen at 10 pc for over 0.1 Gyr (Fig. 13*b*). However, these are rather optimistically young ages for M5 V stars in the solar neighborhood. A more conservative value of 1 Gyr leads to the conclusion that only the most massive objects—11 M_J and above—could be seen by NICMOS at a distance of 10 pc (Fig. 13*c*).

With the adaptive optics scheme proposed by Angel (1994), both the MMT and the LBT will achieve diffraction-limited resolution ($\sim 0''.025$ and $\sim 0''.014$, respectively, at 0.8 μm) from the ground. Typical star/planet flux ratios which can be achieved for bright enough stars can be as high as $\sim 10^9$. Hence, the two telescopes will have sensitivities comparable to the NICMOS cameras at $\lambda = 0.8$ μm (Fig. 9) and may successfully tackle the problem of scattered light. The requirement of a bright central star for accurate wave-front corrections excludes all M dwarfs in the solar neighborhood. The LBT should be able to detect the reflected light of EGPs around all stars of earlier spectral types, regardless of the mass or the age of the planet, as long as the orbital radius a is not too large (Fig. 11*d*). Resolving the planet and the star should be easy for any realistic a within 10 pc. The MMT is about 10 times less sensitive than the LBT, and the combination of parameters that it can usefully search is limited to A-type stars (Fig. 12), or objects so young that they are unlikely to be found in the solar neighborhood. The sensitivity of the LBT in the N band is limited by local thermal background, and its potential for detecting the thermal emission of EGPs is considerably reduced at this wavelength. For EGPs orbiting stars of all spectral types (Figs. 10–13) at a distance of 10 pc from the Sun, the LBT should see 1 M_J planets when younger than 0.03 Gyr, and 5 M_J objects would be detectable for up to 0.3 Gyr. A more reasonable age of 1 Gyr for a G2 V star in the solar neighborhood limits the detection of EGPs to $M \gtrsim 12$ M_J. However, the relative youth of A-type stars brings EGPs of masses above 5 M_J within the range of detectability (Fig. 12*c*). The diffraction-limited resolution of the LBT is $\sim 0''.18$ at N, which is sufficient to resolve most systems within 10 pc.

EGPs of 1 M_J that are bright enough to be seen in the mid- to far-infrared by Gemini and SOFIA are much too young to be found in the solar neighborhood. On the other hand, 5 M_J EGPs are visible until they reach ~ 0.5 Gyr, and by the time they are 1 Gyr old, planets more massive than 7 M_J are detectable at 10 pc. The sensitivity of SOFIA is too low to be useful at wavelengths beyond 10 μm. The lower angular resolution of SOFIA ($\sim 1''$ at best at these wavelengths) limits useful searches to favorable systems with fairly large orbital radii and well within 10 pc of the Sun. While Gemini and other large ground-based telescopes have high angular resolution in the mid-infrared, it is not clear whether they will be able to achieve the proper level of contrast at small angular separations.

SIRTF will have the highest angular resolution of all space-based instruments in the mid- to far-infrared. Its high sensitivity gives it a real chance of detecting the thermal emission of EGPs in the solar neighborhood. It can detect 5 M_J planets as old as 3 Gyr and for a somewhat younger system of age 1 Gyr, 2 M_J EGPs are accessible. Around an A0 V star in particular, planets down to the mass of Saturn (0.3 M_J) are detectable if orbiting within 10 AU. At 20 AU, the low-mass EGPs are not inflated as much by the absorbed stellar light, and in this case the limit is 1 M_J. SIRTF should be particularly good at searching for EGPs around M dwarfs which are too faint in reflected light to be seen by other powerful instruments such as NICMOS and the LBT. Its expected angular resolution of $\sim 1''$–$2''$ limits searches to favorable combinations of distance d and orbital radius a. We cannot presently address the issue of the contrast achievable with the SIRTF telescope and cameras.

The first EGP may well be discovered with *ISO*, which was successfully launched in 1995. Its 5–20 μm sensitivity is not much lower than that of SIRTF, and it should see 3 M_J planets around stars younger than 1 Gyr. Around the necessarily younger A0 stars, 0.3 M_J planets are within reach. The reduced star/planet flux ratio obtained around M stars could result in a successful search for EGPs of 3 M_J and above. The angular resolution of *ISO* is limited by its small aperture (0.6 m) and is further compromised by a pointing jitter of $2''.8$ (*ISO* Observer's Manual 1994). This limits searches to stars within about 5 pc of the Sun. The potential for detection is real, since this leaves ~ 40 candidate stars to search.

We have selected four nearby stars as representative targets in search programs for EGPs: α Lyrae (Vega), τ Ceti, ϵ Eridani, and Gliese 699 (Barnard's star). In each case, we have calculated the evolution of 0.5, 1, and 3 M_J EGPs with $a = 5.2$ AU. Spectral type and parameters required for the calculation are given in Table 1 for each star. These stars were selected to cover the full range of main-sequence spectral types found in the solar neighborhood and for the interest they have previously aroused regarding the possibility of planetary companions.

Vega is an A0 V star with an infrared excess caused by the presence of dust particles in orbit. Spectra for EGPs orbiting Vega are shown in Figure 15*a*, in which we adopt an age of 0.2 Gyr. An EGP companion to Vega could soon be detected. All observing platforms considered here are sensitive enough to detect EGPs of any mass around Vega. The angular dimension of a 5.2 AU orbit spans $0''.67$ at Vega's distance of 7.72 pc, which is below the angular resolution of *ISO*, SIRTF, and SOFIA. Doubling the separation to 10 AU would bring it within reach of SIRTF. Instruments sensitive to reflected light (MMT, LBT, and NICMOS) will easily resolve the EGP for any plausible separation.

Walker et al. (1995) have monitored τ Cet and ϵ Eri for radial velocity variations of very small amplitude during a 12 yr period. While they obtained a marginal indication of a companion to ϵ Eri, they did not detect any companion of planetary mass around the 21 stars of their survey. Because the orbital plane may be inclined to the line of sight, their analysis does not exclude EGPs of masses up to 2–3 M_J, with orbital periods from several years to over a decade. The shortest orbital period we anticipate for an EGP is based on the radius at which water ice condenses in the protoplanetary disk. Using the disk model of Wood & Morfill (1988), supplemented with the assumptions given in § 4.2, we find that the shortest period should be ~ 10 yr. The disk model of Boss (1995) is consistent with this lower limit on the orbital periods of EGPs. The existence of EGPs with such long periods is mildly constrained by the 12 yr study of Walker et al. (1995).

The target of several searches for extraterrestrial intelligence, τ Ceti is a nearby solar-type star. Its main-sequence lifetime is long, and it shows no sign of chromospheric activity. Considering that the median age of stars in the solar neighborhood is 2 Gyr, we adopt a slightly older age of 3 Gyr for this calculation (Fig. 15*b*). The star is at 3.50 pc, and a Jupiter-like separation would subtend a $1''.5$ angle, too small for *ISO* to resolve. The MMT, LBT, and NICMOS will easily detect and resolve EGPs of all masses around τ Cet. SIRTF is sensitive enough to see a 3 M_J planet beyond $\lambda = 8$ μm. At this wavelength, a diffraction-

TABLE 1

CHARACTERISTICS OF THE NEARBY STARS OF FIGURE 15

Star	Type	$L/L_\odot$	d (pc)	Age[a] (Gyr)
α Lyr	A0 V	80	7.72	0.2
τ Cet	G8 V	0.59	3.50	3
ϵ Eri	K2 V	0.34	3.27	1
Gl 699[b]	M4 V	0.0034	1.83	3

[a] Approximate age adopted for the calculation shown in Fig. 15.

[b] Barnard's star.

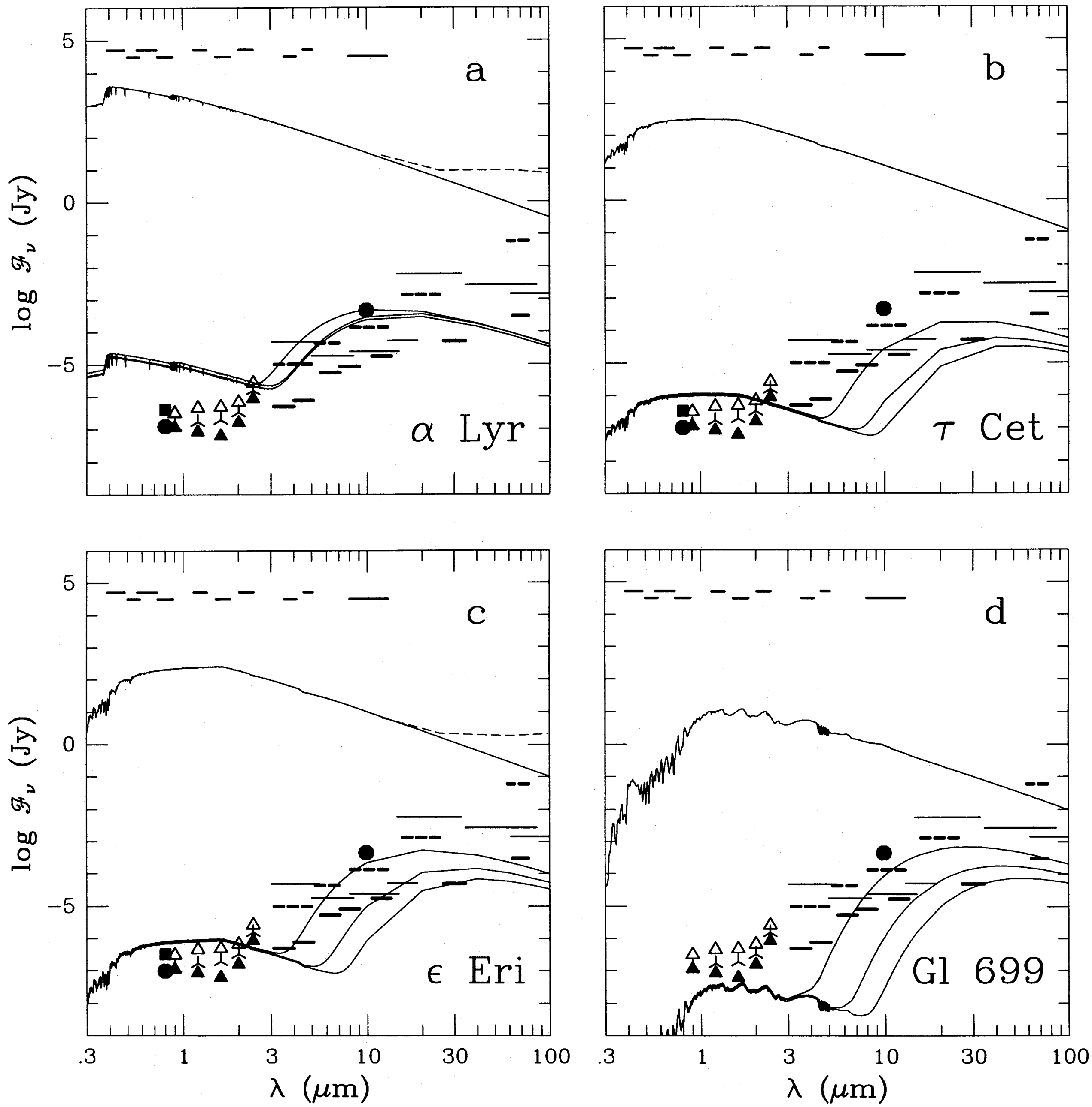

FIG. 15.—Spectral flux from hypothetical EGPs orbiting at $a = 5.2$ AU from specific nearby stars (see Table 1). The spectra correspond to EGPs of 0.5, 1, and 3 M_J (*right to left*). (*a*) α Lyr (Vega); (*b*) τ Cet; (*c*) ϵ Eri; and (*d*) Gl 699 (Barnard's star). The stellar spectra are shown to scale. The far-infrared excesses of α Lyr and ϵ Eri observed by *IRAS* are shown by dashed lines (Gillett 1986). Other symbols are the same as in Fig. 9.

limited resolution of only $\sim 2''$ would require a separation slightly larger than 5.2 AU to resolve the system.

With a mass of only $\sim 0.8\ M_\odot$, ϵ Eridani has a very long main-sequence life and could potentially be very old. However, its level of chromospheric activity and its far-infrared excess are signs of youth, and we assign it an approximate age of 1 Gyr (Fig. 15*c*). EGPs orbiting ϵ Eri would therefore be brighter than around τ Cet. At 3.27 pc from the Sun, ϵ Eri is somewhat closer than τ Cet, and the star/planet separation is 1″.6 for a 5.2 AU orbit. Again, reflected starlight will be easily detected by the MMT, the LBT, and NICMOS. The younger age assumed for ϵ Eri brings 1 M_J EGPs within reach of SIRTF and *ISO*. While *ISO* will not be able to resolve the system, SIRTF could do so if $a > 7$ AU.

Barnard's star (Gl 699) was long thought to have an astrometric companion (van de Kamp 1986), but modern measurements have not confirmed the perturbations originally reported (Heintz 1994). Nevertheless, at 1.83 pc, it is the second nearest stellar system known (the closest being the α Cen triple system), and it is an interesting target. There is no indication of chromospheric activity in this star, and we assume that it is fairly old at 3 Gyr (Fig. 15*d*). Barnard's star is too faint to be a viable target for the adaptive optics system planned for the MMT and LBT. The light reflected by the EGP is too feeble for the NICMOS cameras. SIRTF could easily see a 1 M_J planet at 5.2 AU around Gl 699, since the corresponding angular separation is 2″.84. *ISO* could be equally successful if the system contained an EGP with mass greater than 2 M_J and was slightly wider. Detectability is also favored by the greatly reduced contrast in the mid-infrared, which is $\sim 10^4$–10^5.

Both the Hyades and the Pleiades have been suggested as possible hunting grounds for extrasolar planetary systems. However, searches in these clusters may be in vain, at least in the near future. The Hyades form a fairly old cluster (0.6 Gyr) and are located 45 pc away from the Sun.The Pleiades, on the other hand, are nearly 3 times more distant at 126 pc, but are much younger at 0.07 Gyr (but see Basri, Marcy, & Graham 1995). Our calculation shows that the youth of the Pleiades far outweighs the larger distance, since the bolometric luminosities of EGPs in the Pleiades would be 10–20 times larger than those of their cousins in the Hyades. In a few bandpasses, the flux can be up to 2 orders of magnitude larger. However, the relatively large distances of these two clusters impair EGP searches. In the Hyades, only the NICMOS cameras 1 and 2 have sufficient angular resolution to resolve a planet from its parent star (the stars are too faint to be viable targets for the MMT and LBT), and they will be able to see only very massive EGPs ($\gtrsim 12$ M_J). The problem of resolution is even more acute in the more distant Pleiades, where only the NICMOS camera 1 will be able to resolve EGPs, and only if $a \gtrsim 8$ AU. This instrument should reveal objects with $M > 7$ M_J. Note that brown dwarfs, which are more massive, much brighter, and could form in isolation, should be easily detected by NICMOS, *ISO*, and SIRTF in these two clusters. The large arrays of the SIRTF cameras are very advantageous for such a program.

4.4. *Detection of EGPs via Transits of Primaries*

The radii of EGPs will generally lie in the range 80,000–100,000 km, depending on mass, age, and luminosity of the primary. A EGP with an age of 0.1 Gyr orbiting a main-sequence solar-type star will have a radius of approximately 90,000 km, or about 0.13 of its primary (Fig. 4*b*). At the same time, its effective temperature will lie in the range 300–900 K (for a mass in the range 1–10 M_J), or about 0.05–0.15 of the primary's $T_{\rm eff}$. A transit of the primary by the EGP observed at optical wavelengths would thus lead to a maximum light-curve depth of perhaps 1.6%. This is essentially the most favourable case for detecting EGPs orbiting solar-type stars in this fashion. But even for a Jupiter-class object at the present age of Jupiter, the maximum light-curve depth remains at about 1.0%.

An EGP orbiting an A0 V star at 10 AU will have a radius of about 90,000 km at 0.1 Gyr, although Saturn-mass EGPs could have radii in excess of 100,000 km. Taking the main-sequence radius of the A0 primary to be 1.1×10^6 km, the EGP would thus have a radius 0.08 times that of the primary, leading to a light-curve depth of 0.6%, not greatly inferior to the situation for solar-type primaries.

In the case where an EGP orbits a very late main-sequence star with $M = 0.2$ $M_\odot$ and $T_{\rm eff} = 3330$ K, a transit of the M dwarf by the EGP would lead to a high-amplitude light curve, for the EGPs radius would be in excess of 60% of the primary's.

We confirm the analysis of Borucki & Genet (1992), which shows that EGPs could be detected via transits of main-sequence primaries. In general, an EGP will have a radius which is an appreciable fraction of the primary's radius, as is the case for Jupiter, and most EGPs will have radii somewhat larger than Jupiter's. In most cases transits could be reliably detected via photometry of the primary star at suitably chosen wavelengths, with a relative precision of $\sim 10^{-3}$.

5. CONCLUSIONS

We have constructed a broad suite of models of extrasolar giant planets, ranging in mass from 0.3 to 15 M_J. The models predict luminosity (both reflected and emitted) as a function of age, mass, deuterium abundance, and distance from parent stars of various spectral type. We also explored the effect of variations in helium mass fraction and rotation rate, and the effect of the presence of a rock-ice core.

The models employ the most accurate available equation of state for the interior and boundary conditions interpolated between those of our previously published brown dwarf atmospheres (Burrows et al. 1993), and models optimized for low effective temperatures (GPGO). This enables us to predict with some confidence the radii of these objects as a function of mass and time, and to characterize accurately the inflation effect associated with illumination by the parent star.

Some of the primary conclusions of our study are as follows:

1. Objects below 12 M_J do not undergo deuterium fusion; we propose this limit as one way to distinguish brown dwarfs from EGPs (but we recognize that there are other distinguishing characteristics). For plausible values of the deuterium abundance in stars in the solar neighborhood, a deuterium main sequence ($f_N = 1$) is not obtained.
2. The interaction between illumination from the parent star and the radius of an EGP can lead to evolutionary histories distinctly different from those of isolated objects. Parent star illumination is important primarily for stars of solar and earlier spectral type. M dwarfs do not inflate EGPs at all for plausible orbital distances; except for reflected light, the behavior of EGPs around M dwarfs is virtually identical to that of isolated EGPs.
3. The brightness contrast between an EGP and its parent star is a parameter of primary importance in gauging detectability. In the visible to near-infrared this ratio varies, primarily because of the surface area of the EGP and its distance from the parent star. Because the radius as a function of mass has a broad maximum around 4 M_J, the light reflected by EGPs is a very weak function of the mass. In contrast, the thermal emission and hence the brightness contrast in the 3–15 μm region of the spectrum vary sharply with mass: a doubling of the mass from 1 to 2 M_J can decrease the star-planet contrast by an order of magnitude. Star-planet contrasts in the thermal infrared as low as 30 are found in some of our more massive EGP models, enormously more favorable than the value of 10^9 found in the optical for a Jupiter orbiting a G2 V star a 5 AU (a standard case for studies of planet searches).
4. The biggest challenge facing discovery of EGPs around nearby stars is the small angular separation (0″.5–2″) between parent star and EGP, leading to the requirement for high effective angular resolution in direct detection strategies. Large ground-based telescopes such as the MMT and proposed LBT, configured for adaptive-optics systems, along with the air/spaceborne systems SOFIA, *ISO*, SIRTF, and NICMOS on *HST*, are collectively capable of detecting EGPs in the presence of parent star glare for much of the parameter space of wavelength, stellar spectral type, EGP mass, and age explored here. Additionally, instruments

designed to detect transits of stars by EGPs should do best for M dwarfs, provided they have sufficient photon sensitivity. Because each individual facility is capable of detection in a much smaller volume of this parameter space, we recommend that any planet-search program utilize a variety of facilities over a broad range of wavelengths. From the ground, observations should be conducted in the *B*, *V*, *R*, *I*, *M*, and *N* bands, while space-based observations should favor the 20–30 μm region, where the emission of EGPs is expected to be maximized.

We close by emphasizing that the present set of models represents a significant improvement over previous studies in the mass range considered here. Black's (1980) pioneering models rely on the 12 M_J model of GG73 to construct a power-law relation for $L(M, t)$ and $R(M, t)$; because of the inaccuracy of this model, Black's relation overestimates luminosities by an order of magnitude and radii by 50% for 10 M_J-class models, becoming increasingly more accurate for less massive and older objects.

In spite of the careful treatment of boundary condition and interior physics, the present models represent only an intermediate step. Two major improvements required are (1) to treat the atmospheric thermal and reflected energy balance in a nongray fashion, considering explicitly the frequency dependence of molecular absorptions and (2) to model the properties of clouds for these atmospheres.

To understand the complexity associated with these problems, consider the evolution of an atmosphere as its effective temperature decreases from 1500 to 150 K (Lunine et al. 1986). At roughly 1500 K silicate clouds condense and contribute opacity; these sink deeper into the interior as $T_{\rm eff}$ drops. As $T_{\rm eff}$ decreases below 1000 K, methane and additional water are formed at the expense of carbon monoxide, changing the atmospheric opacity. As the effective temperature drops below 200–300 K, molecular nitrogen converts to gaseous ammonia, and additionally water clouds condense around the 1 bar pressure level; both of these changes greatly affect the thermal and reflected opacity structures. Finally, the formation of ammonia clouds in the upper atmosphere at around Jupiter's effective temperature has a strong effect on reflected appearance.

Clearly, to model these changes accurately is a daunting challenge, but illustrative of the richness of EGPs as a class of astrophysical objects. Positive detections of such objects around nearby stars will intensify interest in such models; for now it is hoped the present comprehensive set of models will provide useful insights for the search.

We cannot present here all possible combinations of parameters of potential interest. A more complete set of tables is available on the Theoretical Astrophysics Program home page (URL: http://lepton.physics.arizona.edu:8000). Investigators who require further models should contact one of the authors to arrange for specific calculations.

Note added in manuscript (*1995 November 16*).—In a recent study of the structure of giant planets at very small orbital separations from the central star (Guillot et al. 1996), we find that the stellar heating causes a radiative zone to develop at the surface of the EGP. As a consequence, the inflation is not as pronounced as reported here for fully convective structures (§ 3.2).

We acknowledge useful discussions with R. Angel, T. Henry, D. Hunten, J. Liebert, G. Rieke, D. Sandler, G. Schneider, A. Sprague, and N. Woolf. We are also grateful to G. Bjoraker for providing the IR spectrum of Jupiter shown in Figure 10. This work was supported by NSF grant AST-9318970, NASA grant NAG5-2817, and by NASA grant HF-1051.01-93A from the Space Telescope Science Institute, which is operated by the Association of Universities for Research in Astronomy, Inc., under NASA contract NAS5-26555. T. G. acknowledges support from the European Space Agency.

APPENDIX

TABLES OF FLUXES AND APPARENT MAGNITUDES

Tables 2–6 give fluxes (in janskys) received at the Earth for selected models. The fluxes are based on the approximations given in § 4, and the transmission curves of Bessell & Brett (1988) and Bessell (1990) define the *V*–*M* photometric bandpasses. The *N* bandpass is on the IRTF system (A. Tokunage 1994, private communication).

TABLE 2

PLANET ORBITING AT 5.2 AU FROM A G2 V STAR AT 10.0 pc FROM EARTH

		log $\mathcal{F}_\nu$ (Jy)							
M/M_J	log t	V	R	I	J	H	K	M	N
0.299	7.50	−6.65	−6.56	−6.52	−6.52	−6.59	−6.80	−6.57	−4.63
	8.00	−6.74	−6.66	−6.62	−6.62	−6.68	−6.89	−7.38	−5.42
	8.50	−6.82	−6.73	−6.69	−6.69	−6.76	−6.97	−7.51	−6.24
	9.00	−6.87	−6.79	−6.74	−6.74	−6.81	−7.02	−7.57	−7.08
	9.50	−6.89	−6.80	−6.76	−6.76	−6.82	−7.04	−7.58	−7.43
	9.70	−6.89	−6.80	−6.76	−6.76	−6.83	−7.04	−7.58	−7.45
0.500	7.50	−6.65	−6.57	−6.53	−6.53	−6.59	−6.81	−5.65	−4.17
	8.00	−6.73	−6.64	−6.60	−6.60	−6.66	−6.88	−6.95	−4.88
	8.50	−6.79	−6.70	−6.66	−6.66	−6.72	−6.94	−7.46	−5.69
	9.00	−6.84	−6.75	−6.71	−6.71	−6.78	−6.99	−7.54	−6.59
	9.50	−6.87	−6.78	−6.74	−6.74	−6.81	−7.02	−7.56	−7.28
	9.70	−6.87	−6.79	−6.75	−6.75	−6.81	−7.02	−7.57	−7.39
0.700	7.50	−6.66	−6.58	−6.54	−6.54	−6.60	−6.81	−5.01	−3.87
	8.00	−6.72	−6.64	−6.60	−6.60	−6.66	−6.87	−6.28	−4.51
	8.50	−6.77	−6.69	−6.65	−6.65	−6.71	−6.93	−7.35	−5.30
	9.00	−6.82	−6.74	−6.70	−6.70	−6.76	−6.97	−7.52	−6.20
	9.50	−6.85	−6.77	−6.73	−6.73	−6.79	−7.01	−7.55	−7.06
	9.70	−6.86	−6.78	−6.74	−6.74	−6.80	−7.01	−7.56	−7.28
1.000	7.50	−6.68	−6.59	−6.55	−6.55	−6.61	−6.69	−4.38	−3.57
	8.00	−6.73	−6.65	−6.60	−6.60	−6.67	−6.88	−5.61	−4.19
	8.50	−6.77	−6.69	−6.65	−6.65	−6.71	−6.92	−7.02	−4.95
	9.00	−6.81	−6.73	−6.69	−6.69	−6.75	−6.96	−7.49	−5.78
	9.50	−6.84	−6.76	−6.72	−6.72	−6.78	−7.00	−7.54	−6.71
	9.70	−6.85	−6.77	−6.73	−6.73	−6.79	−7.00	−7.55	−7.03
1.200	7.50	−6.68	−6.60	−6.56	−6.56	−6.61	−6.45	−4.11	−3.44
	8.00	−6.73	−6.65	−6.61	−6.61	−6.67	−6.88	−5.28	−4.03
	8.50	−6.77	−6.69	−6.64	−6.64	−6.71	−6.92	−6.75	−4.78
	9.00	−6.81	−6.72	−6.68	−6.68	−6.74	−6.96	−7.47	−5.58
	9.50	−6.84	−6.75	−6.71	−6.71	−6.77	−6.99	−7.53	−6.50
	9.70	−6.85	−6.76	−6.72	−6.72	−6.78	−7.00	−7.54	−6.85
1.500	7.50	−6.68	−6.60	−6.56	−6.56	−6.59	−6.02	−3.84	−3.30
	8.00	−6.73	−6.65	−6.60	−6.60	−6.67	−6.87	−4.92	−3.86
	8.50	−6.77	−6.68	−6.64	−6.64	−6.70	−6.92	−6.38	−4.58
	9.00	−6.80	−6.72	−6.67	−6.68	−6.74	−6.95	−7.38	−5.32
	9.50	−6.83	−6.75	−6.70	−6.71	−6.77	−6.98	−7.53	−6.23
	9.70	−6.84	−6.76	−6.71	−6.72	−6.78	−6.99	−7.54	−6.59
2.000	7.50	−6.68	−6.60	−6.56	−6.55	−6.42	−5.39	−3.51	−3.14
	8.00	−6.73	−6.64	−6.60	−6.60	−6.66	−6.77	−4.49	−3.65
	8.50	−6.76	−6.68	−6.64	−6.64	−6.70	−6.91	−5.82	−4.31
	9.00	−6.79	−6.71	−6.67	−6.67	−6.73	−6.94	−7.10	−5.01
	9.50	−6.82	−6.74	−6.70	−6.70	−6.76	−6.97	−7.51	−5.87
	9.70	−6.83	−6.75	−6.71	−6.71	−6.77	−6.98	−7.53	−6.24
3.000	7.50	−6.68	−6.59	−6.55	−6.48	−5.64	−4.54	−3.10	−2.92
	8.00	−6.72	−6.64	−6.59	−6.59	−6.64	−6.17	−3.93	−3.37
	8.50	−6.76	−6.67	−6.63	−6.63	−6.69	−6.90	−5.07	−3.94
	9.00	−6.78	−6.70	−6.66	−6.66	−6.72	−6.94	−6.41	−4.61
	9.50	−6.81	−6.73	−6.69	−6.69	−6.75	−6.96	−7.42	−5.39
	9.70	−6.82	−6.74	−6.70	−6.70	−6.76	−6.98	−7.50	−5.72
5.000	7.50	−6.67	−6.58	−6.54	−5.53	−4.39	−3.56	−2.63	−2.66
	8.00	−6.72	−6.63	−6.59	−6.57	−6.06	−4.92	−3.30	−3.05
	8.50	−6.76	−6.67	−6.63	−6.63	−6.69	−6.55	−4.21	−3.53
	9.00	−6.79	−6.70	−6.66	−6.66	−6.72	−6.94	−5.48	−4.16
	9.50	−6.81	−6.73	−6.69	−6.69	−6.75	−6.96	−6.71	−4.77
	9.70	−6.82	−6.74	−6.70	−6.70	−6.76	−6.97	−7.20	−5.10
10.000	7.50	−6.64	−6.16	−5.33	−3.61	−2.90	−2.44	−2.09	−2.34
	8.00	−6.74	−6.65	−6.57	−5.07	−4.03	−3.31	−2.55	−2.65
	8.50	−6.79	−6.71	−6.67	−6.56	−5.65	−4.56	−3.17	−3.02
	9.00	−6.83	−6.75	−6.71	−6.71	−6.76	−6.47	−4.17	−3.54
	9.50	−6.85	−6.77	−6.73	−6.73	−6.79	−7.00	−5.63	−4.26
	9.70	−6.86	−6.77	−6.73	−6.73	−6.80	−7.01	−6.00	−4.44

TABLE 3

PLANET ORBITING AT 10.0 AU FROM A G2 V STAR AT 10.0 pc FROM EARTH

		log $\mathcal{F}_\nu$ (Jy)							
M/M_J	log t	V	R	I	J	H	K	M	N
0.299	7.50	−7.22	−7.13	−7.09	−7.09	−7.16	−7.37	−6.66	−4.64
	8.00	−7.31	−7.23	−7.19	−7.19	−7.25	−7.47	−7.86	−5.46
	8.50	−7.40	−7.31	−7.27	−7.27	−7.33	−7.55	−8.09	−6.41
	9.00	−7.46	−7.37	−7.33	−7.33	−7.40	−7.61	−8.16	−7.60
	9.50	−7.50	−7.41	−7.37	−7.37	−7.44	−7.65	−8.19	−8.48
	9.70	−7.51	−7.42	−7.38	−7.38	−7.45	−7.66	−8.20	−8.62
0.500	7.50	−7.22	−7.14	−7.10	−7.10	−7.16	−7.37	−5.66	−4.17
	8.00	−7.29	−7.21	−7.17	−7.17	−7.23	−7.45	−7.10	−4.90
	8.50	−7.36	−7.27	−7.23	−7.23	−7.29	−7.51	−8.00	−5.75
	9.00	−7.42	−7.33	−7.29	−7.29	−7.35	−7.57	−8.11	−6.84
	9.50	−7.46	−7.37	−7.33	−7.33	−7.40	−7.61	−8.15	−8.04
	9.70	−7.47	−7.39	−7.34	−7.34	−7.41	−7.62	−8.17	−8.36
1.000	7.50	−7.25	−7.16	−7.12	−7.12	−7.18	−6.99	−4.36	−3.56
	8.00	−7.30	−7.21	−7.17	−7.17	−7.23	−7.45	−5.61	−4.19
	8.50	−7.34	−7.26	−7.21	−7.22	−7.28	−7.49	−7.18	−4.96
	9.00	−7.38	−7.30	−7.26	−7.26	−7.32	−7.53	−8.05	−5.87
	9.50	−7.42	−7.33	−7.29	−7.29	−7.35	−7.57	−8.11	−7.01
	9.70	−7.43	−7.35	−7.30	−7.30	−7.37	−7.58	−8.13	−7.53
2.000	7.50	−7.25	−7.16	−7.12	−7.11	−6.69	−5.41	−3.51	−3.14
	8.00	−7.29	−7.21	−7.17	−7.17	−7.23	−7.14	−4.49	−3.65
	8.50	−7.33	−7.25	−7.20	−7.20	−7.27	−7.48	−5.84	−4.31
	9.00	−7.36	−7.28	−7.24	−7.24	−7.30	−7.51	−7.27	−5.02
	9.50	−7.39	−7.31	−7.27	−7.27	−7.33	−7.54	−8.07	−5.95
	9.70	−7.40	−7.32	−7.28	−7.28	−7.34	−7.56	−8.10	−6.38
3.000	7.50	−7.24	−7.16	−7.12	−6.89	−5.68	−4.54	−3.10	−2.92
	8.00	−7.29	−7.20	−7.16	−7.16	−7.15	−6.24	−3.94	−3.37
	8.50	−7.32	−7.24	−7.20	−7.20	−7.26	−7.45	−5.08	−3.95
	9.00	−7.35	−7.27	−7.23	−7.23	−7.29	−7.50	−6.46	−4.61
	9.50	−7.38	−7.30	−7.26	−7.26	−7.32	−7.53	−7.84	−5.43
	9.70	−7.39	−7.31	−7.27	−7.27	−7.33	−7.54	−8.04	−5.78
4.000	7.50	−7.24	−7.15	−7.11	−6.23	−4.94	−3.97	−2.83	−2.77
	8.00	−7.29	−7.20	−7.16	−7.15	−6.76	−5.48	−3.57	−3.19
	8.50	−7.32	−7.24	−7.20	−7.20	−7.26	−7.22	−4.58	−3.71
	9.00	−7.35	−7.27	−7.22	−7.23	−7.29	−7.50	−5.89	−4.35
	9.50	−7.38	−7.29	−7.25	−7.25	−7.32	−7.53	−7.33	−5.06
	9.70	−7.39	−7.30	−7.26	−7.26	−7.33	−7.54	−7.82	−5.40
6.000	7.50	−7.24	−7.14	−6.96	−5.03	−3.98	−3.25	−2.48	−2.58
	8.00	−7.29	−7.20	−7.16	−6.86	−5.61	−4.49	−3.10	−2.94
	8.50	−7.33	−7.24	−7.20	−7.20	−7.15	−6.12	−3.90	−3.37
	9.00	−7.36	−7.28	−7.24	−7.24	−7.30	−7.49	−5.13	−3.99
	9.50	−7.39	−7.30	−7.26	−7.26	−7.32	−7.54	−6.44	−4.62
	9.70	−7.40	−7.31	−7.27	−7.27	−7.33	−7.55	−7.04	−4.92
8.000	7.50	−7.23	−6.93	−6.17	−4.18	−3.34	−2.77	−2.25	−2.44
	8.00	−7.30	−7.21	−7.16	−5.88	−4.66	−3.78	−2.76	−2.76
	8.50	−7.35	−7.26	−7.22	−7.19	−6.48	−5.21	−3.47	−3.16
	9.00	−7.38	−7.30	−7.26	−7.26	−7.32	−7.20	−4.56	−3.73
	9.50	−7.40	−7.32	−7.28	−7.28	−7.34	−7.56	−6.00	−4.43
	9.70	−7.41	−7.33	−7.29	−7.29	−7.35	−7.56	−6.44	−4.64
10.000	7.50	−7.13	−6.30	−5.35	−3.61	−2.90	−2.44	−2.09	−2.34
	8.00	−7.31	−7.21	−7.02	−5.08	−4.03	−3.31	−2.55	−2.65
	8.50	−7.36	−7.28	−7.24	−6.93	−5.68	−4.57	−3.17	−3.02
	9.00	−7.40	−7.31	−7.27	−7.27	−7.30	−6.58	−4.17	−3.54
	9.50	−7.42	−7.34	−7.30	−7.30	−7.36	−7.57	−5.64	−4.27
	9.70	−7.43	−7.34	−7.30	−7.30	−7.36	−7.58	−6.02	−4.45

TABLE 4

Planet Orbiting at 10.0 AU from a A0 V Star at 10.0 pc from Earth

		log $\mathcal{F}_\nu$ (Jy)							
M/M_J	log t	V	R	I	J	H	K	M	N
0.299	7.00	−5.43	−5.50	−5.60	−5.78	−5.97	−6.17	−5.08	−3.83
	7.50	−5.52	−5.59	−5.69	−5.87	−6.07	−6.27	−5.91	−4.28
	8.00	−5.56	−5.63	−5.73	−5.91	−6.10	−6.30	−6.27	−4.49
	8.30	−5.56	−5.64	−5.74	−5.92	−6.11	−6.31	−6.31	−4.52
0.500	7.00	−5.49	−5.56	−5.66	−5.84	−6.03	−6.17	−4.37	−3.52
	7.50	−5.56	−5.64	−5.74	−5.92	−6.11	−6.31	−5.35	−4.03
	8.00	−5.61	−5.69	−5.79	−5.97	−6.16	−6.36	−6.11	−4.43
	8.30	−5.63	−5.70	−5.80	−5.98	−6.17	−6.37	−6.32	−4.55
1.000	7.00	−5.54	−5.61	−5.71	−5.89	−5.85	−5.12	−3.42	−3.07
	7.50	−5.60	−5.68	−5.78	−5.96	−6.14	−6.22	−4.29	−3.54
	8.00	−5.65	−5.72	−5.82	−6.00	−6.19	−6.39	−5.33	−4.07
	8.30	−5.67	−5.74	−5.84	−6.02	−6.21	−6.42	−5.91	−4.35
2.000	7.00	−5.55	−5.62	−5.72	−5.65	−4.65	−3.88	−2.79	−2.74
	7.50	−5.61	−5.68	−5.78	−5.96	−5.92	−5.19	−3.49	−3.14
	8.00	−5.65	−5.73	−5.83	−6.01	−6.20	−6.30	−4.42	−3.63
	8.30	−5.67	−5.75	−5.85	−6.03	−6.22	−6.41	−5.05	−3.95
3.000	7.00	−5.55	−5.62	−5.72	−4.94	−3.91	−3.27	−2.48	−2.56
	7.50	−5.60	−5.68	−5.78	−5.91	−5.26	−4.42	−3.09	−2.92
	8.00	−5.65	−5.72	−5.82	−6.00	−6.16	−5.85	−3.90	−3.37
	8.30	−5.67	−5.74	−5.84	−6.02	−6.21	−6.34	−4.49	−3.67
4.000	7.00	−5.54	−5.61	−5.67	−4.31	−3.41	−2.87	−2.28	−2.44
	7.50	−5.60	−5.67	−5.77	−5.67	−4.66	−3.90	−2.82	−2.77
	8.00	−5.65	−5.72	−5.82	−6.00	−5.98	−5.26	−3.55	−3.18
	8.30	−5.67	−5.74	−5.84	−6.02	−6.20	−6.07	−4.09	−3.47
6.000	7.00	−5.53	−5.52	−5.12	−3.45	−2.76	−2.35	−2.01	−2.27
	7.50	−5.60	−5.67	−5.76	−4.82	−3.82	−3.21	−2.48	−2.58
	8.00	−5.65	−5.72	−5.82	−5.93	−5.22	−4.38	−3.09	−2.94
	8.30	−5.67	−5.75	−5.85	−6.02	−5.97	−5.22	−3.54	−3.19
8.000	7.00	−5.47	−5.08	−4.33	−2.88	−2.33	−2.02	−1.83	−2.15
	7.50	−5.60	−5.66	−5.64	−4.07	−3.24	−2.75	−2.25	−2.44
	8.00	−5.66	−5.73	−5.83	−5.49	−4.43	−3.72	−2.76	−2.77
	8.30	−5.69	−5.76	−5.86	−5.98	−5.30	−4.46	−3.15	−2.99
10.000	7.00	−5.12	−4.35	−3.60	−2.40	−1.97	−1.73	−1.68	−2.05
	7.50	−5.60	−5.60	−5.21	−3.54	−2.85	−2.44	−2.09	−2.34
	8.00	−5.67	−5.74	−5.83	−4.88	−3.88	−3.27	−2.55	−2.65
	8.30	−5.70	−5.78	−5.88	−5.72	−4.69	−3.94	−2.90	−2.86

TABLE 5

PLANET ORBITING AT 20.0 AU FROM A A0 V STAR AT 10.0 pc FROM EARTH

M/M_J	log t	V	R	I	J	H	K	M	N
				log $\mathcal{F}_\nu$ (Jy)					
0.299	7.00	−6.05	−6.13	−6.23	−6.41	−6.60	−6.80	−5.29	−3.94
	7.50	−6.17	−6.24	−6.34	−6.52	−6.71	−6.91	−6.43	−4.54
	8.00	−6.25	−6.32	−6.42	−6.60	−6.79	−6.99	−7.37	−5.13
	8.30	−6.28	−6.35	−6.45	−6.63	−6.82	−7.02	−7.56	−5.40
0.500	7.00	−6.09	−6.17	−6.27	−6.45	−6.64	−6.68	−4.44	−3.55
	7.50	−6.18	−6.25	−6.35	−6.53	−6.73	−6.93	−5.58	−4.14
	8.00	−6.25	−6.32	−6.42	−6.60	−6.79	−6.99	−6.79	−4.76
	8.30	−6.28	−6.35	−6.45	−6.63	−6.82	−7.02	−7.36	−5.12
1.000	7.00	−6.14	−6.21	−6.31	−6.48	−6.11	−5.16	−3.43	−3.07
	7.50	−6.21	−6.28	−6.38	−6.56	−6.74	−6.62	−4.34	−3.56
	8.00	−6.26	−6.33	−6.43	−6.61	−6.80	−7.00	−5.53	−4.16
	8.30	−6.28	−6.36	−6.46	−6.64	−6.83	−7.03	−6.37	−4.57
2.000	7.00	−6.15	−6.23	−6.33	−5.89	−4.67	−3.89	−2.79	−2.74
	7.50	−6.21	−6.29	−6.39	−6.56	−6.19	−5.24	−3.51	−3.14
	8.00	−6.26	−6.33	−6.43	−6.61	−6.80	−6.75	−4.47	−3.65
	8.30	−6.28	−6.35	−6.45	−6.63	−6.82	−7.01	−5.19	−4.01
3.000	7.00	−6.15	−6.22	−6.31	−4.98	−3.91	−3.27	−2.49	−2.56
	7.50	−6.21	−6.28	−6.38	−6.39	−5.32	−4.44	−3.10	−2.93
	8.00	−6.25	−6.32	−6.42	−6.60	−6.68	−5.99	−3.93	−3.38
	8.30	−6.27	−6.35	−6.45	−6.63	−6.81	−6.81	−4.55	−3.70
4.000	7.00	−6.14	−6.21	−6.15	−4.32	−3.41	−2.87	−2.28	−2.44
	7.50	−6.20	−6.28	−6.37	−5.89	−4.68	−3.90	−2.83	−2.78
	8.00	−6.25	−6.32	−6.42	−6.59	−6.26	−5.31	−3.56	−3.19
	8.30	−6.27	−6.34	−6.44	−6.62	−6.77	−6.30	−4.12	−3.49
6.000	7.00	−6.12	−5.94	−5.22	−3.46	−2.76	−2.36	−2.01	−2.27
	7.50	−6.20	−6.27	−6.34	−4.85	−3.83	−3.21	−2.48	−2.58
	8.00	−6.25	−6.32	−6.42	−6.38	−5.26	−4.40	−3.10	−2.95
	8.30	−6.28	−6.35	−6.45	−6.62	−6.21	−5.25	−3.54	−3.19
8.000	7.00	−5.94	−5.20	−4.35	−2.88	−2.33	−2.02	−1.83	−2.15
	7.50	−6.20	−6.24	−5.99	−4.08	−3.25	−2.75	−2.25	−2.44
	8.00	−6.26	−6.33	−6.43	−5.61	−4.44	−3.72	−2.76	−2.77
	8.30	−6.29	−6.36	−6.46	−6.44	−5.33	−4.46	−3.15	−2.99
10.000	7.00	−5.28	−4.37	−3.60	−2.40	−1.97	−1.73	−1.68	−2.05
	7.50	−6.19	−6.02	−5.31	−3.54	−2.85	−2.44	−2.09	−2.34
	8.00	−6.27	−6.34	−6.41	−4.90	−3.88	−3.28	−2.55	−2.65
	8.30	−6.30	−6.38	−6.48	−5.91	−4.70	−3.94	−2.90	−2.86

TABLE 6

Planet Orbiting at 2.6 AU from a M5 V Star at 10.0 pc from Earth

		log $\mathcal{F}_\nu$ (Jy)							
M/M_J	log t	V	R	I	J	H	K	M	N
0.299	7.50	−9.31	−8.87	−8.31	−7.72	−7.70	−7.80	−6.70	−4.65
	8.00	−9.75	−9.30	−8.75	−8.15	−8.13	−8.23	−8.26	−5.48
	8.50	−10.04	−9.59	−9.04	−8.45	−8.42	−8.52	−9.02	−6.47
	9.00	−10.10	−9.66	−9.10	−8.51	−8.49	−8.59	−9.10	−7.85
	9.50	−10.16	−9.71	−9.16	−8.57	−8.54	−8.64	−9.15	−9.37
0.500	7.50	−9.31	−8.87	−8.32	−7.72	−7.70	−7.80	−5.67	−4.17
	8.00	−9.72	−9.28	−8.73	−8.13	−8.11	−8.21	−7.18	−4.91
	8.50	−10.00	−9.55	−9.00	−8.40	−8.38	−8.48	−8.72	−5.78
	9.00	−10.06	−9.61	−9.06	−8.47	−8.44	−8.54	−9.05	−6.95
	9.50	−10.10	−9.66	−9.11	−8.51	−8.49	−8.59	−9.10	−8.49
	9.70	−10.12	−9.68	−9.12	−8.53	−8.50	−8.61	−9.12	−9.15
1.000	7.50	−9.34	−8.89	−8.34	−7.75	−7.71	−7.12	−4.37	−3.56
	8.00	−9.73	−9.28	−8.73	−8.14	−8.11	−8.20	−5.63	−4.19
	8.50	−9.98	−9.53	−8.98	−8.39	−8.36	−8.47	−7.26	−4.97
	9.00	−10.02	−9.57	−9.02	−8.43	−8.40	−8.51	−8.83	−5.90
	9.50	−10.06	−9.61	−9.06	−8.47	−8.44	−8.54	−9.05	−7.15
	9.70	−10.07	−9.63	−9.07	−8.48	−8.46	−8.56	−9.07	−7.74
2.000	7.50	−9.34	−8.90	−8.34	−7.71	−6.80	−5.41	−3.51	−3.14
	8.00	−9.72	−9.28	−8.72	−8.13	−8.09	−7.37	−4.50	−3.65
	8.50	−9.97	−9.52	−8.97	−8.38	−8.35	−8.45	−5.85	−4.31
	9.00	−10.00	−9.55	−9.00	−8.41	−8.38	−8.49	−7.39	−5.04
	9.50	−10.03	−9.58	−9.03	−8.44	−8.41	−8.52	−8.90	−5.99
	9.70	−10.04	−9.60	−9.04	−8.45	−8.43	−8.53	−9.02	−6.44
3.000	7.50	−9.34	−8.89	−8.34	−7.15	−5.69	−4.54	−3.10	−2.92
	8.00	−9.72	−9.27	−8.72	−8.12	−7.73	−6.26	−3.94	−3.37
	8.50	−9.96	−9.52	−8.96	−8.37	−8.34	−8.23	−5.08	−3.95
	9.00	−9.99	−9.54	−8.99	−8.40	−8.37	−8.48	−6.48	−4.62
	9.50	−10.02	−9.57	−9.02	−8.43	−8.40	−8.51	−8.20	−5.45
	9.70	−10.03	−9.58	−9.03	−8.44	−8.41	−8.52	−8.75	−5.81
4.000	7.50	−9.33	−8.88	−8.30	−6.28	−4.94	−3.97	−2.83	−2.77
	8.00	−9.72	−9.27	−8.72	−8.06	−6.91	−5.49	−3.57	−3.19
	8.50	−9.96	−9.51	−8.96	−8.37	−8.32	−7.53	−4.58	−3.71
	9.00	−9.99	−9.54	−8.99	−8.40	−8.37	−8.47	−5.90	−4.35
	9.50	−10.02	−9.57	−9.02	−8.42	−8.40	−8.50	−7.47	−5.09
	9.70	−10.03	−9.58	−9.03	−8.43	−8.41	−8.51	−8.15	−5.42
6.000	7.50	−9.31	−8.51	−7.44	−5.03	−3.98	−3.25	−2.48	−2.58
	8.00	−9.72	−9.27	−8.71	−7.12	−5.62	−4.50	−3.10	−2.94
	8.50	−9.97	−9.52	−8.97	−8.36	−7.69	−6.14	−3.90	−3.38
	9.00	−10.00	−9.55	−9.00	−8.41	−8.38	−8.23	−5.08	−3.97
	9.50	−10.02	−9.58	−9.02	−8.43	−8.41	−8.51	−6.48	−4.64
	9.70	−10.03	−9.59	−9.03	−8.44	−8.42	−8.52	−7.11	−4.93
8.000	7.50	−8.82	−7.33	−6.22	−4.19	−3.34	−2.77	−2.25	−2.44
	8.00	−9.73	−9.23	−8.45	−5.90	−4.66	−3.78	−2.76	−2.76
	8.50	−9.98	−9.54	−8.98	−8.07	−6.53	−5.20	−3.46	−3.16
	9.00	−10.02	−9.57	−9.02	−8.43	−8.37	−7.41	−4.55	−3.72
	9.50	−10.04	−9.60	−9.04	−8.45	−8.42	−8.52	−6.01	−4.43
	9.70	−10.05	−9.60	−9.05	−8.46	−8.43	−8.54	−6.49	−4.65
10.000	7.50	−7.76	−6.36	−5.35	−3.61	−2.90	−2.44	−2.09	−2.34
	8.00	−9.70	−8.66	−7.50	−5.07	−4.03	−3.31	−2.55	−2.64
	8.50	−10.00	−9.55	−8.99	−7.20	−5.68	−4.56	−3.17	−3.01
	9.00	−10.04	−9.59	−9.04	−8.44	−8.12	−6.63	−4.17	−3.54
	9.50	−10.06	−9.61	−9.06	−8.47	−8.44	−8.52	−5.65	−4.27
	9.70	−10.06	−9.62	−9.07	−8.47	−8.45	−8.55	−6.07	−4.47

REFERENCES

Allard, F., & Hauschildt, P. H. 1995, ApJ, 445, 433
Angel, J. R. P. 1994, Nature, 368, 203
Angle, R. 1995, private communication
Backman, D. E., Gillett, F. C., & Witteborn, F. C. 1992, ApJ, 385, 670
Basri, G., Marcy, G. W., & Graham, J. R. 1995, ApJ, submitted
Beichman, C. 1995, private communication
Bessell, M. S. 1990, PASP, 102, 1181
Bessell, M. S., & Brett, J. M. 1988, PASP, 100, 1134
Black, D. C. 1980, Icarus, 43, 293
Borucki, W. J., & Genet, R. M. 1992, in ASP Conf. Ser. 34, Robotic Telescopes in the 1990s, ed. A. V. Filippenko (San Francisco: ASP), 153
Boss, A. P. 1986, in Astrophysics of Brown Dwarfs, ed. M. C. Kafatos, R. S. Harrington, & S. P. Maran (Cambridge: Cambridge Univ. Press), 206
———. 1995, Science, 267, 360
Brami, B., Hansen, J. P., & Joly, F. 1979, Physica A, 95, 505
Burrows, A., Hubbard, W. B., Saumon, D., & Lunine, J. I. 1993, ApJ, 406, 158
Burrows, A., Saumon, D., Guillot, T., Hubbard, W. B., & Lunine, J. I. 1995, Nature, 375, 299
Chabrier, G. 1990, J. de Phys., 51, 1607
———. 1995, in preparation
Chabrier, G., & Ashcroft, N. W. 1990, Phys. Rev. A, 42, 2284
Chabrier, G., & Schatzman, E., eds. 1994, The Equation of State in Astrophysics (Cambridge: Cambridge Univ. Press)
Chamberlain J. W., & Hunten, D. M. 1987, Theory of Planetary Atmospheres (Orlando: Academic), 210
Conrath, B. J., Hanel, R. A., & Samuelson, R. E. 1989, in Origin and Evolution of Planetary and Satellite Atmospheres, ed. S. K. Atreya, J. B. Pollack, & M. S. Matthew (Tucson: Univ. Arizona Press), 513
DeWitt, H. E., Chabrier, G., & Slattery, W. L. 1995, in preparation
Dreiling, L. A., & Bell, R. A. 1980, ApJ, 241, 736
Eibl, A, 1995, private communication
Eisenhart, P. 1995, private communication
Ferriso C. C., Ludwig, C. B., & Thomson, A. L. 1966, J. Quant. Spectrosc. Radiat. Transfer, 6, 241
Gatewood, G. D. 1987, AJ, 97, 1189
Gillett, F. C. 1986, in Light on Dark Matter, ed. F. P. Israel (Dordrecht: Riedel), 61
Gould, A., & Loeb, A. 1992, ApJ, 396, 104
Graboske, H. C., Jr., Pollack, J. B., Grossman, A. S., & Olness, R. J. 1975, ApJ, 199, 265 (GPGO)
Grossman, A. S., & Graboske, H. C., Jr. 1973, ApJ, 180, 195 (GG73)
Guillot, T., Burrows, A., Hubbard, W. B., Lunine, J. I., & Saumon, D. 1996, ApJ, in press
Guillot, T., Chabrier, G., Gautier, D., & Morel, P. 1995, ApJ, 450, 463
Guillot, T., Chabrier, G., Morel, P., & Gautier, D. 1994, Icarus, 112, 354
Guillot, T., & Morel, P. 1995, A&AS, 109, 109
Hanel, R., et al. 1979, Science, 204, 972
Heintz, W. D. 1994, AJ 108, 2338
Henry, T. 1995, private communication
Holmes, N. C., Ross, M., & Nellis, W. J. 1995, Phys. Rev. B, in press
Hubbard, W. B. 1977, Icarus, 30, 305
Hubbard, W. B., & Stevenson, D. J. 1984, in Saturn, ed. T. Gehrels & M. S. Matthews (Tucson: Univ. Arizona Press), 47
Hunten, D. M., Tomasko, M., & Wallace, L. 1980, Icarus, 43, 143
ISO Observer's Manual, Version 2.0. 1994, prepared by the *ISO* Science Operations Team, 6
ISOCAM Observer's Manual, Version 1.0. 1994, prepared by the ISOCAM Team
ISOPHOT Observer's Manual, Version 3.1. 1994, prepared by the ISOPHOT consortium, ed. U. Klaas, H. Krüger, I. Heinrichsen, A. Heske, & R. Laureijs, ESA
Jancovici, B. 1977, J. Stat. Phys., 17, 357
Karkoschka, E. 1994, Icarus, 111, 174
Kirkpatrick, J. D., & McCarthy, D. W., Jr. 1994, AJ, 107, 333
Kurucz, R. L. 1993, private communication
Lin, D. N. C., & Papaloizou, J. C. B. 1993, in Protostars and Planets III, ed. E. H. Levy & J. I. Lunine (Tucson: Univ. Arizona Press), 749
Linsky, J. L. 1969, ApJ, 156, 989
Lissauer, J. J. 1995, Icarus, 114, 217
Lunine, J. I., Hubbard, W. B., & Marley, M. S. 1986, ApJ, 310, 238
McMillan, R. S., Moor, T. L., Perry, M. L., & Smith, P. H. 1994, Ap&SS, 212, 271
Mihalas, D. 1978, Stellar Atmospheres (2d ed.; San Francisco: Freeman), § 1.3
Moroz, V. I. 1983, in Venus, ed. D. M. Hunten, L. Colin, T. M. Donahue, & V. I. Moroz (Tucson: Univ. Arizona Press), 27
Nellis, W. J., Ross, M., & Holmes, N. C. 1995, Science, 269, 1249
Podolak, M., Hubbard, W. B., & Pollack, J. B. 1993, in Protostars and Planets III, ed. E. H. Levy & J. I. Lunine (Tucson: Univ. Arizona Press), 1109
Salpeter, E. E. 1973, ApJ, 181, L183
Saumon, D., Chabrier, G., & Van Horn, H. M. 1995, ApJS, 99, 713 (SCVH)
Saumon, D., Hubbard, W. B., Chabrier, G., & Van Horn, H. M. 1992, ApJ, 391, 827
Schneider, G. 1995, private communication
Stevenson, D. J., & Salpeter, E. E. 1977a, ApJS, 35, 221
———. 1977b, ApJS, 35, 239
van de Kamp, P. 1986, Space Sci. Rev., 43, 211
Van Horn, H. M., & Ichimaru, S., ed. 1993, Strongly Coupled Plasma Physics (Rochester: Univ. Rochester Press)
Walker, G. A. H., Walker, A. R., Irwin, A. W., Larson, A. M., Yang, S. L. S., & Richardson, D. C. 1995, Icarus, 116, 359
Wetherill, G. 1993, in Lunar Planet. Sci. Conf. 24, 1511
Wood, J. A., & Morfill, G. E. 1988, in Meteorites and the Early Solar System, ed. J. F. Kerridge & M. S. Matthews (Tucson: Univ. Arizona), 329
Zuckerman, B., Forveille, T., & Kastner, J. H. 1995, Nature, 373, 494